

Near-Infrared Diffuse Correlation Spectroscopy for Assessment of Tissue Blood Flow

Guoqiang Yu

University of Kentucky

Turgut Durduran

Institute of Photonic Sciences

Chao Zhou

Massachusetts Institute of Technology

Ran Cheng

University of Kentucky

Arjun G. Yodh

University of Pennsylvania

10.1	Introduction	195
10.2	Near-Infrared DCS Technology Development	196
10.3	Fundamentals of Diffuse Correlation Spectroscopy.....	197
	Single Scattering • Multiple Scattering Limit (DWS) • Correlation Diffusion Equation (DCS)	
10.4	DCS Technology	200
	DCS System • Fiber-Optic Probes	
10.5	Validation Work.....	203
	DCS versus Doppler Ultrasound in Premature Infant Brain • DCS versus ASL-MRI in Human Muscle	
10.6	In Vivo Applications of DCS	204
	Cancer Therapy Monitoring • Cerebral Physiology and Disease • Skeletal Muscle Hemodynamics	
10.7	Summary.....	211
	Acknowledgments.....	212
	Grant Acknowledgments.....	212
	References.....	212

10.1 Introduction

Microvascular blood flow (BF) delivers nutrients such as oxygen (O_2) to tissue and removes metabolic by-products from tissue. Normal microvascular BF is thus critical for tissue function. Abnormal BF is associated with conditions such as cardiovascular disease, stroke, head trauma, peripheral arterial disease (PAD), and cancer (Yu et al. 2005a, b, 2006, Durduran et al. 2009b, Zhou et al. 2009). Therefore, measurement of BF holds potential to provide useful information for diagnosis of tissue disease and for monitoring therapeutic effects.

The ideal BF measurement should provide quantitative information about macro- and microvasculature with millisecond temporal resolution. The measurements should be carried out continuously, noninvasively, and without risk to subjects. Furthermore, ideal measurements would not be limited to the tissue surface, i.e., it is desirable to probe BF in deep tissues. Unfortunately, no such ideal modality exists. We thus begin with a brief review of the “imperfect” technologies currently utilized in the clinic.

A variety of noninvasive methods are employed for the measurement of BF and blood cell velocity (Wintermark et al. 2005). Ultrasound, for example, penetrates through the skin, making

transcutaneous flow measurements practical. When a cellular target recedes from the fixed sound source, the frequency of the reflected sound wave is lowered because of the Doppler effect (Hoskins 1990). For small changes, the fractional change in sound wave frequency equals the fractional change in cell velocity. Doppler ultrasound can image large vessels in three dimensions with relatively high spatial (~mm) and temporal (~ms) resolution. Unfortunately, this technique is limited to large vessels; extension to the microvasculature requires exogenous contrast agents such as microbubbles (Sehgal et al. 2000, Yu et al. 2005b, Sunar et al. 2007).

Other imaging techniques have been developed to evaluate tissue hemodynamics at the level of the microvasculature (Wintermark et al. 2005), including positron emission tomography (PET) (Baron 1999), single photon emission computed tomography (SPECT) (Mahagne et al. 2004), xenon-enhanced computed tomography (XeCT) (Latchaw et al. 2003), dynamic perfusion computed tomography (PCT) (Wintermark et al. 2000), dynamic susceptibility contrast MRI (DSC-MRI) (Kidwell et al. 2003), and arterial spin labeling magnetic resonance imaging (ASL-MRI) (Detre et al. 1992, Williams et al. 1992). These techniques use endogenous (ASL-MRI) and exogenous tracers (PET, SPECT, XeCT, PCT, and DSC-MRI), and

their temporal and spatial resolutions vary. For example, the data acquisition time for ASL-MRI, PCT, and DSC-MRI is in the range of seconds to minutes, approximately 10 times faster than the other techniques. The spatial resolution for PCT, DSC-MRI, and ASL-MRI can be as small as 2 mm and is typically 4–6 mm.

All of these medical diagnostics, however, have limitations that preclude their routine use in the clinic. PET, SPECT, and xenon-CT require exposure to ionizing radiation, and PET and SPECT require arterial blood sampling for quantification of BF. The MRI methods cannot be used in patients with pacemakers, metal implants, or claustrophobia. Furthermore, most (if not all) of these imaging methods are costly and employ major nonportable instrumentation, requiring patient transport. The methods are largely incompatible with serial measurements and so tend to be used only once in the patient's hospitalization, typically in association with a specific research protocol.

Other surface-sensitive imaging techniques for the measurement of microvascular flow include scanning laser Doppler (Liu et al. 1997), laser speckle imaging (Dunn et al. 2001, Durduran et al. 2004a), and Doppler optical coherence tomography (DOCT) (Chen et al. 1998). These methods are used primarily for noninvasive monitoring of BF in tissues located within a few hundred microns below the tissue surface.

It should be apparent, from the discussion above, that a major unfilled niche remains as per the quest for an "ideal" monitor: "bedside" measurement of BF in deep tissues. To this end, near-infrared (NIR) diffuse optical technologies (Gopinath et al. 1993, Hielscher et al. 1993, Chance 1998, Chance et al. 1998, Fantini et al. 1999, Durduran et al. 2002, Wolf et al. 2003, Yu et al. 2003, Choe et al. 2009, Li et al. 2009) provide a fast and portable alternative to the more costly medical diagnostics (e.g., MRI or CT). A well-known spectral window exists in the NIR (700–900 nm), wherein tissue absorption is relatively low, so that light can penetrate into deep/thick volumes of tissue (up to several centimeters). Traditional near-infrared spectroscopy (NIRS) has long been used for continuous measurements of hemoglobin concentration, blood oxygen saturation, and, indirectly, for BF assessment using exogenous tracers (e.g., indocyanine green dye; Kuebler 2008). The present chapter is concerned with a qualitatively different technique for the measurement of BF. The technique was originally introduced for the study of complex fluids and was dubbed diffusing-wave spectroscopy (DWS) (Maret and Wolf 1987, Pine et al. 1988, Stephen 1988, Maret 1997); more recently, diffuse correlation spectroscopy (DCS) (Boas et al. 1995, Boas and Yodh 1997), a differential formulation of DWS, has been developed and vigorously applied to probe BF in deep tissue vasculature. The aforementioned photon-correlation methods share the advantages of NIRS (i.e., deep/thick tissue penetration), but provide a more direct and robust measure of BF (Boas et al. 1995, Boas 1996, Boas and Yodh 1997, Cheung et al. 2001, Durduran 2004, Durduran et al. 2004b, Li et al. 2005, Yu et al. 2005a,b, 2006, Zhou et al. 2007, Durduran et al. 2009b, Shang et al. 2009).

DCS offers several attractive new features for BF measurement. Among these features are noninvasiveness (i.e., no ionizing radiation, no contrast agents), high-temporal resolution (up to 100 Hz) (Dietsche et al. 2007), and relatively large penetration depth (up to several centimeters) (Durduran et al. 2004b, Li et al. 2005). On the other hand, DCS has relatively poor spatial resolution, about 0.5 mm near the surface and degrades with depth. For measurement in adult humans, DCS holds potential to provide information complementary to that available from imaging techniques that measure tissue morphology, such as MRI, or tissue function, such as PET. Perhaps, most importantly, DCS can be easily deployed at the bedside in the clinic (Yu et al. 2006, Durduran et al. 2009b) and, therefore, can be utilized for continuous monitoring.

In this chapter, we sketch the historical development and physical basis of DCS. We then describe DCS instrumentation and provide examples of its validation. Finally, we provide some in vivo application examples. This chapter is not intended to discuss every detail of every problem; rather, it is intended to provide a flavor for the method and a snap-shot of recent progress.

10.2 Near-Infrared DCS Technology Development

Near-infrared diffuse optical spectroscopies naturally separate into "static" and "dynamic" regimes. Here, we use the terms "static" and "dynamic" to distinguish methods that probe the motions of scatterers. NIRS is a "static" method; it primarily measures the relatively slow variations in tissue absorption and scattering. The most common applications of NIRS focus on the measurement of oxy- and deoxy-hemoglobin concentration. These concentrations are then utilized to derive microvascular total hemoglobin (THC) concentration and blood oxygen saturation. Very fast NIRS methods (Fantini et al. 1999, Wolf et al. 2003) have been employed to measure rapid (~100 Hz) changes in tissue scattering, but we nevertheless still refer to these methods as "static," since they probe changes in the "amount of scattering" rather than scatterer motion. "Dynamic" methods, on the other hand, directly measure the motions of scatterers (Tanaka et al. 1974, Stern 1975, Feke and Riva 1978, Maret and Wolf 1987, Pine et al. 1988, Stephen 1988, Tong et al. 1988, Boas et al. 1995, Boas and Yodh 1997). In the case of tissues, the critical moving scatterers are red blood cells (RBCs). The dynamic or correlation methods achieve this goal, typically using coherent sources and monitoring temporal statistics (or frequency-domain analogs of temporal statistics) of the speckle fluctuations of the scattered light. In most of these dynamic experiments, the electric field temporal autocorrelation function or its Fourier transform is measured. The detected signal is related to the motion of the RBCs, and BF can be derived using a model for photon propagation through tissues.

A well-known and notable methodology for measuring BF is "laser Doppler flowmetry" (Bonner and Nossal 1981). In this

case, pairs of very closely separated (<1 mm) sources and detectors are used to detect single-scattered light from tissue samples. In laser Doppler flowmetry, the frequency-broadening or frequency-shift of the detected speckle fluctuations are fit to a model within the single-scattering approximation. The single-scattering approximation simplifies the experimental analysis, but it also limits the reliability and amount of information that can be extracted from real tissue samples. A related technique is “laser speckle flowmetry” or “laser speckle contrast analysis” (LASCA) (Briers 2001). LASCA utilizes the spatial blurring of speckles during a CCD exposure time to obtain large-field-of-view images of tissue motions in a single shot. Both methods are mostly limited to superficial tissues (~ 1 mm), although recently laser Doppler flowmetry with larger source-detector separations was utilized to extend its reach to ~ 1 cm (Binzoni et al. 2004).

Studies of deep tissues required the development of multiple-scattering models of photon propagation. Various extensions of photon correlation spectroscopy from single- to highly scattering systems were made in the 1980s (Bonner and Nossal 1981, Valkov and Romanov 1986, Bonner et al. 1987, Maret and Wolf 1987, Pine et al. 1988). The technique—dubbed DWS—was developed to study optically dense complex fluids that multiply scattered light. DWS was a brilliant insight that had transformative effects on the soft matter field. From the biomedical optics perspective, a key advance was the development of an understanding of the analogy between correlation transport (Ackerson et al. 1992) and photon transport (in the early-mid 1990s). A theory based on the diffusion equation for temporal correlation transport was first introduced by Boas and coworkers (Boas et al. 1995, Boas and Yodh 1997); they called the technique DCS in order to avoid confusion with terminology associated with diffuse absorption spectroscopy. Applications in biological tissues ensued rapidly thereafter because of the connection thus established between traditional diffuse optics (NIRS) and the diffuse models for transport of electric field temporal autocorrelation functions through turbid media. The DCS technique was thus built on a rigorous mathematical description, which clearly showed how motional fluctuations were impressed upon the temporal correlations of diffuse light fields propagating in tissue. One advantage of the correlation diffusion equation theory over previous theories was the ease with which predictions could be made for turbid media with spatially varying dynamics and optical properties using numerical and analytic tools similar to those of NIRS (see for example, Boas et al. 1995, Boas and Yodh 1997, and Heckmeier et al. 1997).

Instrumentation and application of DCS for in vivo measurements quickly followed this early research (Gisler et al. 1995, 1997, Cheung et al. 2001, Culver et al. 2003a, Durduran et al. 2004b, 2009b, 2005, Li et al. 2005, 2008, Yu et al. 2005a,b, 2006, 2007, Zhou et al. 2006, 2007, 2009, Dietsche et al. 2007, Sunar et al. 2007, Gagnon et al. 2008, 2009, Buckley et al. 2009, Varma et al. 2009, Kim et al. 2010, Roche-Labarbe et al. 2010, Shang et al. 2010, Mesquita et al. 2010, Zirak et al. 2010, Carp et al. 2010, Belau et al. 2010). We next describe the theoretical basis of DCS.

10.3 Fundamentals of Diffuse Correlation Spectroscopy

DCS is an extension of single-scattering dynamic light scattering (DLS) (Berne and Pecora 1990, Chu 1991, Brown 1993) (or quasi-elastic light scattering, QELS) to the multiple scattering limit. DLS has been widely used to study particle suspension properties such as particle size and shape. However, DLS is only applicable to optically thin samples. DCS is a multiple-scattering technique that extends the methodology of DLS to the study of optically thick samples. In this section, we start with a description of single-scattering theory, and then we extend the discussion to the multiple scattering regime. Detailed reviews of the theoretical development for DCS can also be found in the references (Boas et al. 1995, Boas 1996, Boas and Yodh 1997, Durduran 2004, 2010b, Zhou 2007).

10.3.1 Single Scattering

In a single-scattering laboratory sample, photons are usually scattered once (or not at all) before they leave the sample (see Figure 10.1a). A pointlike photon detector is placed at an angle θ relative to the input beam propagation direction. If the scatterers are particle-like objects that move, then the total electric field will vary in time, and intensity fluctuations are observed. The

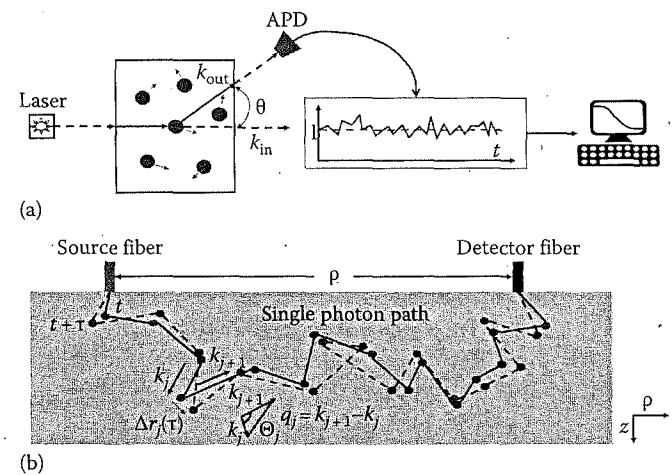


FIGURE 10.1 (a) Illustration schematic of a single-scattering dynamic light-scattering experiment. (b) Schematic of multiple-scattering setup showing a typical photon path through the turbid media. k_j and k_{j+1} are the wave vectors associated with the photon (or electric field) before and after the j th scattering event, respectively. $q_j = k_{j+1} - k_j$ is the scattering wave vector or momentum transfer, and θ_j is the scattering angle of the j th scattering event. The solid line indicates the photon path at time t , while the dotted line represents the photon path at time $t + \tau$. During the delay time τ , the j th scatterer is displaced by $\Delta r_j(\tau)$. Also indicated is the source-detector separation on the sample surface, ρ , and the direction z is defined normal to the sample surface. (From Zhou, C., In-vivo optical imaging and spectroscopy of cerebral hemodynamics, PhD dissertation, University of Pennsylvania, Philadelphia, PA, 2007.)

fluctuations of the electric field and intensity carry information about the dynamic properties of the medium, i.e., the motion of the particles. The normalized temporal autocorrelation function of the scattered electric field ($\mathbf{E}(t)$) is

$$g_1(\tau) = \frac{\langle \mathbf{E}(t) \cdot \mathbf{E}^*(t + \tau) \rangle}{\langle \mathbf{E}(t) \cdot \mathbf{E}^*(t) \rangle} = e^{i\omega\tau} e^{-\frac{1}{2}q^2 \langle \Delta r^2(\tau) \rangle}. \quad (10.1)$$

Here, τ is the autocorrelation delay time, ω is the angular frequency of the input light field, $q^2 = 2k_0^2(1 - \cos\theta)$ is the square of the scattering wavevector, $k_0 = 2\pi n/\lambda$ is the wavevector magnitude of the incident light field, n is the index of refraction of the medium, λ is the wavelength of the light field, and $\langle \Delta r^2(\tau) \rangle$ is the mean square displacement of the scatterers in the medium, which directly characterizes the particle movement. In most experiments, the normalized temporal intensity autocorrelation function, $g_2(\tau) = \langle I(t)I(t + \tau) \rangle / \langle I(t) \rangle^2$, is calculated from the intensity fluctuations of the scattered light. $g_2(\tau)$ is related to the temporal field autocorrelation function, $g_1(\tau)$, through the Siegert relationship (Rice 1954):

$$g_2(\tau) = 1 + \beta |g_1(\tau)|^2, \quad (10.2)$$

where β depends on the detection optics and is inversely proportional to the number of detected speckles or modes. The β value can be determined experimentally for each measurement from the intercept of the intensity autocorrelation function as the delay time τ approaches zero.

10.3.2 Multiple Scattering Limit (DWS)

Multiple scattering effects must be included in applications involving most biological tissues. In this case, each scattering event from a moving scatterer contributes to the accumulation of the phase shift and therefore the decay of the correlation function. If we assume that the field from individual photon paths (see Figure 10.1b) is uncorrelated, the total temporal field autocorrelation function can be expressed as the weighted sum of the field autocorrelation function from each photon path. Furthermore, if we assume a homogeneous medium and further assume that each scattering event is independent and that the scatterer displacements are uncorrelated, the field autocorrelation function from a single path can be written as

$$g_1(\tau)_{\text{onepath}} = e^{i\omega\tau} e^{-\frac{1}{2}k_0^2 Y \langle \Delta r^2(\tau) \rangle}, \quad (10.3)$$

where $Y = N \cdot (1 - \langle \cos \theta \rangle_N)$ and $\langle \cos \theta \rangle_N$ are the average value of cosine over all the N scattering events along the path. When N is large, the average value approaches the ensemble average, $\langle \cos \theta \rangle$, which is usually denoted by the so-called anisotropy factor (g) of the medium. The reduced photon-scattering length or random-walk step length, $l_s^* = 1/\mu_s'$, where μ_s' is the reduced scattering

coefficient of the medium. The photon-scattering length, $l_s = 1/\mu_s$, where μ_s is the scattering coefficient of the medium. Thus, $l_s^* = \frac{1}{\mu_s'} = \frac{1}{\mu_s(1-g)} = \frac{l_s}{1-\langle \cos \theta \rangle}$ (Wolf et al. 1988). Let s represent the total pathlength associated with a particular photon path. Then, the number of scattering events associated with this same path is $N = s/l_s$, and $Y = s/l_s^*$ equals the total number of photon *random-walk* steps associated with the photon path.

The final detected field autocorrelation function contains the contributions of all photon paths. If we use $P(Y)$ to represent the probability distribution for photon paths with a number of random walk steps, Y , then the total electric field autocorrelation function can be computed by incoherently integrating the contributions from each photon path (Maret and Wolf 1987, Middleton and Fisher 1991), i.e.,

$$g_1(\tau) = e^{i\omega\tau} \int_0^{\infty} P(Y) e^{-\frac{1}{2}k_0^2 Y \langle \Delta r^2(\tau) \rangle} dY. \quad (10.4)$$

In a highly scattering medium, Equation 10.4 can be equivalently expressed as an integral over all possible pathlengths using the pathlength distribution (Maret and Wolf 1987, Pine et al. 1988, MacKintosh and John 1989), $P(s)$, i.e.,

$$g_1(\tau) = e^{i\omega\tau} \int_0^{\infty} P(s) e^{-\frac{s}{2l_s^*} k_0^2 \langle \Delta r^2(\tau) \rangle} ds. \quad (10.5)$$

Equation 10.5 is the primary result from DWS for a homogeneous turbid scattering medium composed of moving particle-like scatterers. Note, the DWS correlation function is typically measured at some points inside the sample or on its surface, and $P(s)$ depends implicitly on both measurement location and source position. The distribution of $P(Y)$ can be readily obtained from Monte Carlo simulation (Zhou 2007). Alternatively, derivation of $P(s)$ can be achieved experimentally, e.g., from a time-resolved spectroscopy measurement (Jacques 1989, Patterson et al. 1989, Yodh et al. 1990, Benaron and Stevenson 1993). Analytical solutions for $P(s)$ can also be obtained for simple geometries, such as infinite, semi-infinite, and slab, by solving the photon diffusion equation with appropriate boundary conditions (see Chapter 16).

10.3.3 Correlation Diffusion Equation (DCS)

Later, Boas et al. (Boas et al. 1995, Boas 1996, Boas and Yodh 1997) derived a correlation diffusion equation from correlation transport theory (Ackerson and Pusey 1988, Ackerson et al. 1992). The correlation diffusion equation aptly described the propagation of the unnormalized electric field temporal autocorrelation function in turbid media. This differential equation approach is particularly attractive for investigation of heterogeneous media (Boas et al. 1995, Boas and Yodh 1997, Heckmeier et al. 1997) and provides a natural framework for tomographic

reconstruction of tissue dynamics (Boas and Yodh 1997, Culver et al. 2003a, Zhou et al. 2006). Rather than reproduce the earlier derivations, here, we simply remind the reader about the diffusion equation for photon fluence rate, and then we write out the analogous result for photon-electric field correlation. The rigorous step-by-step derivation of the correlation diffusion equation can be found elsewhere (Boas et al. 1995, Boas 1996, Boas and Yodh 1997).

The well-known photon diffusion equation, which describes the photon propagation in tissue, is indicated below. In highly scattering media, such as tissue, the photon fluence rate, $\Phi(\mathbf{r}, t)$ [$\text{W}\cdot\text{cm}^{-2}$], obeys the time-dependent diffusion equation:

$$\nabla \cdot (D\nabla\Phi(\mathbf{r}, t)) - \nu\mu_a\Phi(\mathbf{r}, t) + \nu S(\mathbf{r}, t) = \frac{\partial\Phi(\mathbf{r}, t)}{\partial t}, \quad (10.6)$$

where

\mathbf{r} is the position vector

t [s] is time

ν [$\text{cm}\cdot\text{s}^{-1}$] is the speed of light in the medium

μ_a [cm^{-1}] is the medium absorption coefficient, and $D \approx \nu/3\mu'_s$ is the photon diffusion coefficient in the medium, where μ'_s [cm^{-1}] is the reduced scattering coefficient of the medium. $S(\mathbf{r}, t)$ [$\text{Watt}\cdot\text{cm}^{-3}$] is the isotropic source term.

It turns out that under essentially the same set of approximations, the *unnormalized* temporal field autocorrelation function, $G_1(\mathbf{r}, \tau) = \langle \mathbf{E}(\mathbf{r}, t) \cdot \mathbf{E}^*(\mathbf{r}, t + \tau) \rangle$, obeys a formally similar diffusion equation, i.e.,

$$\nabla \cdot (D\nabla G_1(\mathbf{r}, \tau)) - (\nu\mu_a + \frac{1}{3}\nu\mu'_s k_0^2 \langle \Delta r^2(\tau) \rangle) G_1(\mathbf{r}, \tau) = -\nu S_0 e^{i\omega\tau} \delta^3(\mathbf{r} - \mathbf{r}_s). \quad (10.7)$$

Here, the source term is continuous wave (CW), and scatterer movement (i.e., $\langle \Delta r^2(\tau) \rangle$) combines with photon absorption to give an *effective* "absorption" term for the attenuation of unnormalized electric field temporal autocorrelation function as it travels through the medium. The formal similarity of Equations 10.6 and 10.7 suggests that their solutions will also be formally similar. In semi-infinite homogeneous media (see Figure 10.2), for example, the solution to Equation 10.7 can be obtained as (Boas 1996)

$$G_1(\rho, \tau) = \frac{\nu S_0 e^{i\omega\tau}}{4\pi D} \left(\frac{e^{-K(\tau)r_1}}{r_1} - \frac{e^{-K(\tau)r_2}}{r_2} \right). \quad (10.8)$$

Here, ρ is the distance between the source and detector fiber,

$$r_1 = \sqrt{\rho^2 + z_0^2}, \quad r_2 = \sqrt{\rho^2 + (z_0 + 2z_b)^2}, \quad z_0 = 1/\mu'_s, \quad z_b = \frac{2}{3\mu'_s} \frac{1 + R_{\text{eff}}}{1 - R_{\text{eff}}},$$

$R_{\text{eff}} = -1.44n^{-2} + 0.71n^{-1} + 0.668 + 0.064n$, is the effective reflection coefficient determined by the ratio of the refraction indices

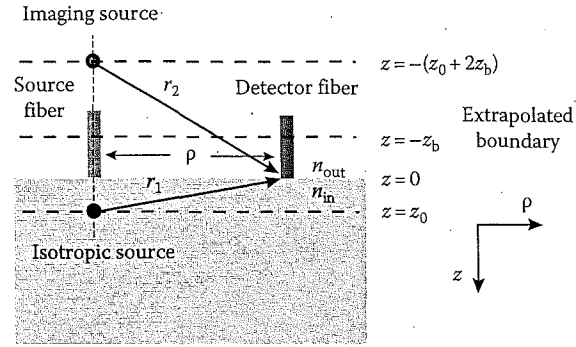


FIGURE 10.2 Illustration of the semi-infinite geometry. The collimated source is usually approximated as an isotropic source located at $z = z_0 = 1/\mu'_s$ into the medium. The boundary condition requirement leads to a signal size of zero (i.e., for fluence rate in the case of a NIR diffuse reflectance measurement or for the temporal autocorrelation function in the case of the DCS measurement) at $z = -z_b = -\frac{2}{3\mu'_s} \frac{1 + R_{\text{eff}}}{1 - R_{\text{eff}}}$, which is generally called the extrapolated zero-boundary condition (Haskell et al. 1994). For the semi-infinite homogeneous geometry, the extrapolated zero boundary condition can be satisfied by considering a negative isotropic imaging source located at $z = -(z_0 + 2z_b)$. (From Zhou, C., In-vivo optical imaging and spectroscopy of cerebral hemodynamics, PhD dissertation, University of Pennsylvania, Philadelphia, PA, 2007.)

inside and outside the medium ($n = n_{\text{in}}/n_{\text{out}}$, see Figure 10.2), and $K^2(\tau) = 3\mu_a\mu'_s + \mu'_s k_0^2 \langle \Delta r^2(\tau) \rangle$.

One other modification of the correlation diffusion equation is required for biological tissues. Generally, biological tissues contain *static* (or very slow moving) scatterers (e.g., organelles and mitochondria) and *moving* scatterers (e.g., RBCs). The scattering events from the static objects in tissue do not contribute significantly to the phase shift and correlation function temporal decay in Equation 10.7. To account for this effect, we introduce a unitless factor, α , which represents the fraction of light-scattering events from "moving" scatterers. Formally, the factor α is included as a prefix to the *effective* "absorption" term in Equation 10.7 (i.e., $\frac{1}{3}\nu\mu'_s k_0^2 \alpha \langle \Delta r^2(\tau) \rangle$), and so it arises as well as in the definition of $K^2(\tau)$ (e.g., $K^2(\tau) = 3\mu_a\mu'_s + \mu'_s k_0^2 \alpha \langle \Delta r^2(\tau) \rangle$). We thus see that the decay of the temporal field correlation function depends on tissue optical properties, μ_a , μ'_s , the mean-square-displacement of the moving scatterers, $\langle \Delta r^2(\tau) \rangle$, and the factor α , which accounts for the presence of static scatterers.

For the case of random ballistic flow, $\langle \Delta r^2(\tau) \rangle = V^2\tau^2$, where V^2 is the second moment of the cell velocity distribution. For the case of diffusive motion, $\langle \Delta r^2(\tau) \rangle = 6D_b\tau$, where D_b is the *effective* Brownian diffusion coefficient of the tissue scatterers and is distinct from the well-known thermal Brownian diffusion coefficient due originally to Einstein (1905). RBCs pass through capillaries in single file and experience shear flow in larger vessels; the RBCs also experience tumbling motions in addition to translation. Intuitively, the random ballistic flow model might be considered the best model with which to fit DCS data. In

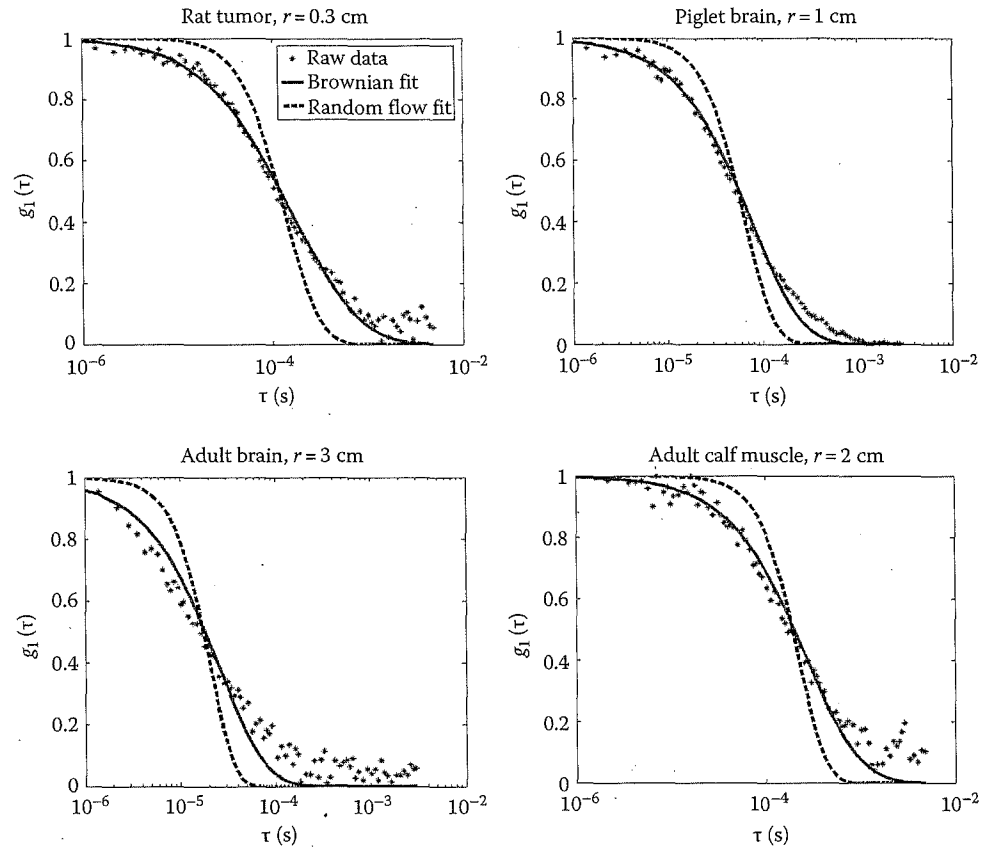


FIGURE 10.3 DCS data (i.e., the normalized electric field autocorrelation function) from a rat tumor, piglet brain, human calf muscle, and adult human brain. The source-detector separations are also indicated on each plot. Dots are experimental data. The dashed line is a fit with $\langle \Delta r^2 \rangle \sim \tau^2$ (random flow), and the solid line is a fit with $\langle \Delta r^2 \rangle \sim \tau$ (Brownian motion). Note, the fitting accuracy depends on the delay time (τ); at the longer delay times, the data tend to deviate further from the fits in the measurements. This effect arises mainly because later delay times in the autocorrelation function are due to the photons that probe the more superficial tissues; the presence of the skull and/or the skin, with its relatively minimal vasculature, therefore alters the long-delay time portion of the autocorrelation functions. (From Zhou, C., In-vivo optical imaging and spectroscopy of cerebral hemodynamics, PhD dissertation, University of Pennsylvania, Philadelphia, PA, 2007.)

practice, however, we have observed that the diffusion model, i.e., $\langle \Delta r^2(\tau) \rangle = 6D_b\tau$, fits the autocorrelation curves rather well over a broad range of tissue types (see Figure 10.3), ranging from rat brain (Cheung et al. 2001, Zhou et al. 2006) and mouse tumor (Menon et al. 2003, Yu et al. 2005b), to piglet brain (Zhou et al. 2009), adult human skeletal muscle (Yu et al. 2005a, Shang et al. 2009), adult human tumors (Sunar et al. 2006, Zhou et al. 2007), premature brain (Buckley et al. 2009, Roche-Labarbe et al. 2010), and adult brain (Durduran et al. 2004b, Li et al. 2005, 2008, Durduran et al. 2009b). The D_b value obtained from such experiments is generally several orders of magnitude larger than the thermal (i.e., Einstein) Brownian diffusion coefficient of RBCs in plasma. The reason for the Brownian-motion-like correlation curves is still not apparent and more investigation is needed to sort through these issues. Nevertheless, an empirical approach has been adopted by researchers in biomedical optics applying DCS for the measurement of tissue BF.

Although the unit of αD_b (cm^2/s) is different from the traditional blood perfusion unit [$\text{mL}/\text{min}/100\text{g}$], changes in this flow-index (αD_b) have been found to correlate quite well with other

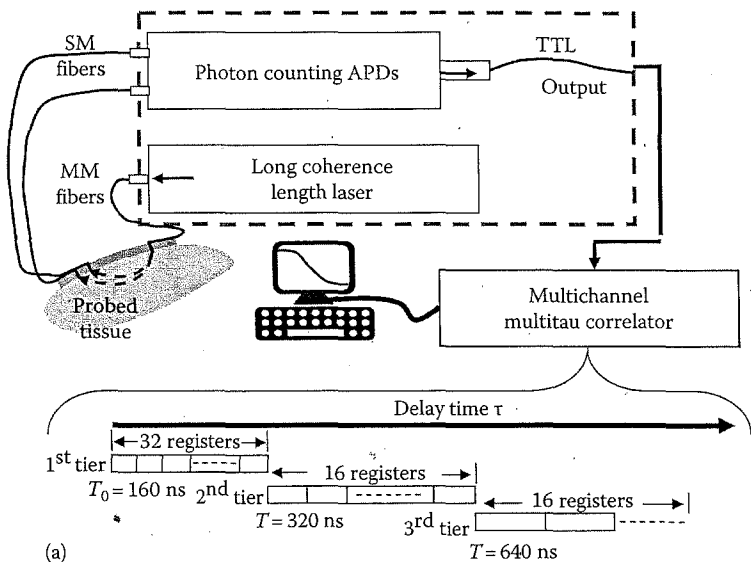
BF measurement modalities (see Section 10.5). Therefore, αD_b is used as the BF index ($\text{BFI} = \alpha D_b$) and relative BF, $r\text{BF} = \text{BFI}/\text{BFI}_0$, where BFI_0 is the measurement at the baseline, is used to indicate relative BF changes for DCS throughout this chapter.

10.4 DCS Technology

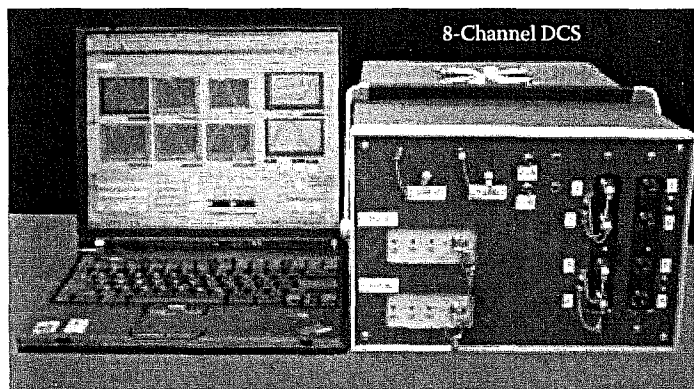
In this section, we briefly review the system design and implementation of DCS technology. Detailed descriptions of specific systems can be found in the references.

10.4.1 DCS System

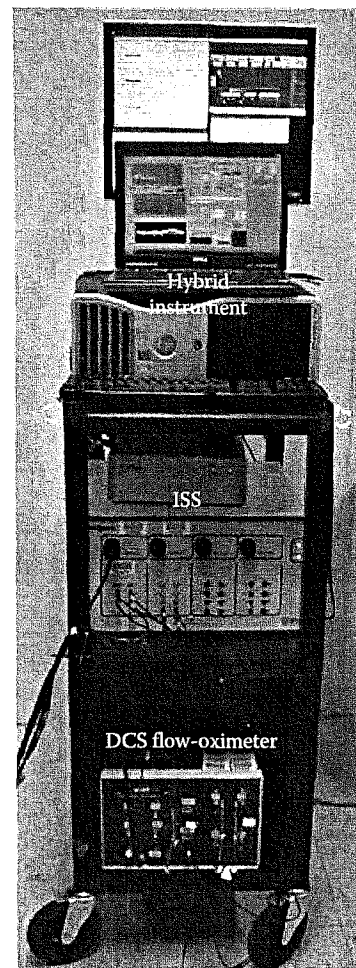
Figure 10.4a shows the diagram of a typical DCS system. A long coherence length laser is required as the light source for DCS. Output from the laser can be delivered to the tissue through a multimode source fiber. Single-mode (or few-mode) fibers should be used to collect photons from a single (or a few) speckle(s). Fast photon-counting avalanche photodiodes (APDs) (typically from Perkin Elmer, CA) are generally used as detectors. A multi- τ



(a)



(b)



(c)

FIGURE 10.4 (a) Schematic diagram of a typical DCS system. (b) A photograph of the eight-channel DCS system. (c) Photograph of a hybrid diffuse optical system consisting of a DCS flow oximeter and a frequency-domain tissue oximeter (From Imagent, ISS Inc.).

correlator board (Correlator.com, NJ) takes the TTL output from the APDs and calculates normalized temporal intensity autocorrelation functions of the detected signal. Since the correlator board is at the heart of the DCS measurements, we will briefly describe its structure and the algorithm used for calculating the correlation curves.

The correlator board utilizes a “multi-tau” scheme for the calculation of the autocorrelation functions. Figure 10.4a shows the structure of a typical multi-tau correlator design. In this case, the first 32 registers (the first tier) of the correlator have a bin width $T_0 = 160$ ns. After that, the bin width doubles every 16 registers. For example, registers 33–48 (the second tier) have a bin width $T = 320$ ns, and registers 49–64 (the third tier) have a bin width $T = 640$ ns. When a measurement starts, a digital counter reports the number of TTL pulses (photon counts) detected within each binning time (160 ns) of the first register. The value in each register is passed to its right as a new value is coming in from the left. Note that a register with a bin width $T = 160$ ns is updated every 160 ns, while the register with a 320 ns bin width

updates every 320 ns, etc. The temporal intensity autocorrelation functions are calculated before each shift. For example, the unnormalized intensity autocorrelation coefficient for the i th register, $G_2(\tau_i)$, is calculated as

$$G_2(\tau_i) = \langle n_i \cdot n_0 \rangle. \tag{10.9}$$

Here

- n_i indicates the photon count in the i th register
- n_0 is the photon count at zero delay time ($\tau = 0$) with the same bin width as the i th register
- τ_i is the delay time between n_i and n_0

The autocorrelation function is continuously averaged over the entire acquisition time t . Note that n_0 is the photon count in the first register when n_i is in the first tier, while n_0 is the summation of the photon count in the first four registers when n_i is in the third tier ($T/T_0 = 4$), etc. The delay time τ_i is calculated as the

summation of all the bin widths on the left of the i th register. Using the multi-tau scheme, a delay time span of many orders of magnitude (i.e., from hundred of nanoseconds to minutes) can be achieved with only a few hundred register channels, and the computation load is greatly reduced compared to a linear autocorrelator.

The DCS technologies have been implemented in tissues by several research groups (Cheung et al. 2001, Culver et al. 2003a, Durduran et al. 2004b, 2005, Li et al. 2005, Yu et al. 2005a,b, Roche-Labarbe et al. 2010, Shang et al. 2009), yielding BF information in animal models and in human subjects/patients. To fully utilize the BF information provided by DCS, hybrid systems combining DCS and NIRS have been demonstrated to provide more comprehensive information for the calculation of tissue BF, blood oxygenation, and oxygenation metabolism (see an example in Figure 10.4c) (Cheung et al. 2001, Culver et al. 2003a, Durduran 2004, Yu et al. 2005a, Roche-Labarbe et al. 2010). In addition, due to the recent development of novel solid-state laser technologies, the DCS system can be made very compact (Zhou et al. 2007, Shang et al. 2009). Figure 10.4b shows an eight-channel DCS instrument, which only measures $18\text{ cm} \times 28\text{ cm} \times 33\text{ cm}$. Very recently, Shang et al. (2009) demonstrated a dual wavelength DCS flow oximeter, which permits tissue BF and oxygenation to be measured simultaneously by a single compact system (bottom of Figure 10.4c). The device is truly portable and is suitable for bedside and *en route* monitoring of tissue hemodynamics.

10.4.2 Fiber-Optic Probes

In an analogous fashion to NIRS, DCS also enables use of a large variety of probes. The most basic probe employs one or more source-fibers (multimode) and one or more detector fibers (single- or few-mode). A key point in DCS is the use of single- or few-mode fibers, which limit the detector fiber diameter to tens of micrometers. We have shown in the past (Zhou et al. 2006) that enlarging the fiber diameter to cover multiple speckles increases the signal intensity but also increases the noise in a proportional fashion, and therefore the signal-to-noise ratio is not necessarily improved. In our laboratories, we routinely employ single-mode

fibers to detect light from a single speckle, and we often bundle 2–8 fibers nearby and detect the collected photons with individual, independent detectors (see Figure 10.4a).

In Figure 10.5, we show three example probes. The first probe (see Figure 10.5a) is a typical probe used in brain and muscle studies on humans (Durduran et al. 2004b, Yu et al. 2005a). Straight, 90 degree bent or side-firing fibers are utilized. This probe can readily be made MRI compatible (Yu et al. 2005a, Durduran et al. 2010a). The second probe (see Figure 10.5b) is a typical “noncontact” probe, where an array of source-detector fibers is placed together at the focal plane of a “camera.” In many experiments, we utilize an old SLR camera; this camera holds a 1:1 imaging lens array and provides a light tight box. In this arrangement, cross-polarizers are often utilized between source and detector fibers to reduce the detrimental effects of surface reflections and single-scattered light. This approach improves the “ β ” value (see Section 10.3) and while we lose photons, we gain in reduced noise (Zhou et al. 2006). Finally, the third type of probe (see Figure 10.5c) shows a surgical device, wherein side-firing fibers were embedded in a catheter, which could be inserted into tissues (Yu et al. 2006) or sutured onto the tissue surface. Practically all ideas from experiences in NIRS can be adapted for DCS use, and the instruments are hybridized by adding extra source and/or detector fibers.

Here, we also highlight a probe utilized by Gisler and coworkers that employ up to 32 few-mode fibers to detect light from multiple speckles simultaneously (Dietsche et al. 2007). Their goal was to maximize the number of detected photons per fiber by utilizing few-mode fibers, which collect data from several speckles and also at the same time acquire many correlation functions in parallel. With this approach, they have reduced the integration time down to 6.5 ms and are able to resolve changes in BF due to arterial pulsation in an analogous fashion to pulse-oximetry. Figure 10.6a and b shows the arrangement of the fibers and collection tip (Dietsche et al. 2007). As shown in Figure 10.6c, they were able to obtain the pulsation dynamics (inset) and some initial insights into the dependence of the shape of the field autocorrelation functions on the pulsatility of the vasculature. This experimental approach may turn out to be useful for improving our understanding of the physical basis of

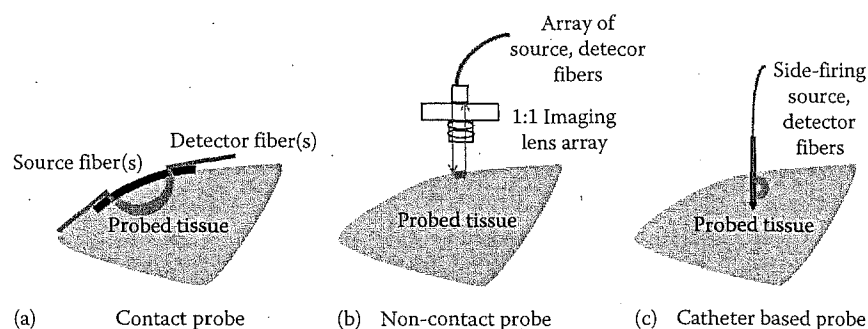


FIGURE 10.5 Three schematic examples of DCS tissue probes: (a) contact probe, (b) noncontact probe, and (c) side-illumination catheter-based probe.

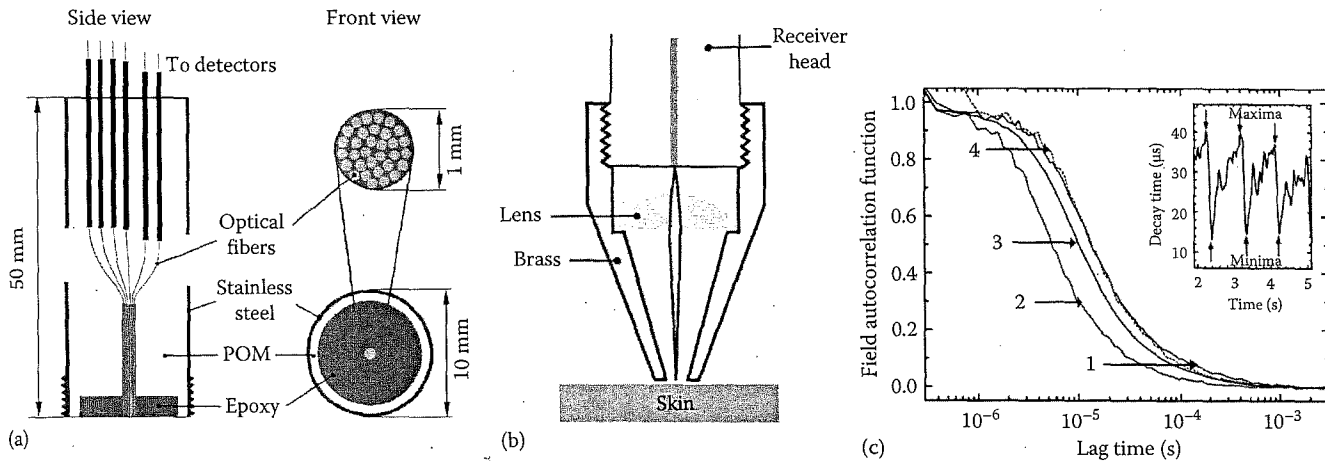


FIGURE 10.6 (a) Side and top views of the multifiber receiver head, (b) receiver head with attached collection optics; and (c) the electric field autocorrelation function $\langle g_j^{(1)}(\tau) \rangle_N$ averaged over N fibers as a function of lag time τ at the diastolic maxima (1) and systolic minima (2) of mean decay time (τ_d) measured at the fingertip. The number of receiver channels is $N=23$. The integration time per field autocorrelation function is 26 ms. Data are averages over 11 field autocorrelation functions measured at the maxima and minima of the τ_d curve (top and bottom, respectively, in inset). (3) $\langle g_j^{(1)}(\tau) \rangle_N$ averaged over 10 s, which mimics the “standard” DCS measurement, where the data are averaged across the heart-beat cycle. For easier comparison with the diastolic data, the systolic field autocorrelation function was shifted in time (4). Note that the shape of the curves are slightly different in a complex manner, possibly indicating different amounts of photon penetration at maxima and minima, differing optical properties and subtle changes in physiology. This is an indication that with further improved understanding of the physical basis of these curves, more information about the underlying physiology may be accessible. (From Dietsche, G. et al., *Appl. Opt.*, 46, 8506, 2007. With permission.)

the detailed shapes of the measured autocorrelation functions. Furthermore, this unique probe may become more popular in the future with increased parallelization of DCS detection and corresponding autocorrelator electronics.

10.5 Validation Work

The biomedical application of DCS for deep tissue measurements of BF is a relatively new development. Therefore, a substantial amount of technique validation work has been carried out, and, arguably, more work is needed to establish its medical uses. This validation research is needed even though the basis of DCS is DWS, a method that has been widely utilized in condensed matter research (Maret 1997). However, DCS application to in vivo measurement of deep tissue BF was (and continues to be) novel and demanded careful examination in this context. During the last decade, DCS measurements of BF variation in various tissues/organs have been compared to other standards, including power Doppler ultrasound in murine tumors (Menon et al. 2003, Yu et al. 2005b), laser Doppler in rat brain (Durduran 2004), xenon-CT in traumatic brain (Kim et al. 2010), Doppler ultrasound in premature infant brain (Buckley et al. 2009, Roche-Labarbe et al. 2010), fluorescent microsphere measurement of cerebral BF in piglet brain (Durduran et al. 2008, Zhou et al. 2009), ASL-MRI in human brain and muscle (Durduran et al. 2004b, Yu et al. 2007), and to reports in the literature (Cheung et al. 2001, Culver et al. 2003a, c, Durduran 2004, Durduran et al. 2005, Dietsche et al. 2007, Li et al. 2008). This validation research has progressed hand-in-hand with

numerical, theoretical studies (Boas et al. 1995, Durduran 2004, Jaillon et al. 2006, Zhou et al. 2006, Zhou 2007, Gagnon et al. 2008, Varma et al. 2009), and with studies of tissue simulating phantoms (Boas et al. 2002, Cheung et al. 2003, Durduran 2004, Zhou 2007), wherein the medium’s viscosity and/or the flow speed of scatterers were varied (Boas 1996, Cheung et al. 2001, Durduran 2004). Overall, these validation studies have shown that DCS measurements of BF variations are in good agreement with theoretical expectation, computer simulation, and other biomedical measurement techniques. Some of these validation studies are described below.

10.5.1 DCS versus Doppler Ultrasound in Premature Infant Brain

Two recent papers (Buckley et al. 2009, Roche-Labarbe et al. 2010) have utilized DCS in prematurely born infants and have compared DCS microvascular BF findings to transcranial Doppler ultrasound measurements of large artery BF velocity. In work by Buckley et al. (2009), the authors monitored very low birth weight, very premature infants during a 12° postural elevation. DCS was used to measure *microvascular* cerebral BF (CBF) and transcranial Doppler ultrasound (TCD) to measure *macrovascular* BF velocity in the middle cerebral artery (Buckley et al. 2009, Roche-Labarbe et al. 2010). Population-averaged DCS and TCD data yielded no significant hemodynamic response to this postural change ($p > 0.05$), indicating overall agreement between the two modalities in response to this mild challenge. More interestingly, *absolute* DCS data

(αD_b) correlated significantly with peak systolic, end diastolic, and mean velocities measured by TCD ($p=0.036$, 0.036 , and 0.047). Roche-Labarbe et al. (2010) have also reported a similar finding ($p=0.04$) comparing *absolute* DCS data to mean velocities measured by TCD. Overall, these two studies demonstrate that DCS has a strong potential for use in premature infants and agrees well with the established TCD measures, despite the fact that the two techniques measure related but different quantities (i.e., microvascular local CBF vs. large artery, global CBF velocity). The studies also suggest that with further understanding of the physical basis of the photon-RBC interactions at the microscopic level, and/or with improved calibration, DCS could be used to measure absolute CBF.

10.5.2 DCS versus ASL-MRI in Human Muscle

The DCS BF measurement was also validated against flow measurements by arterial-spin-labeled perfusion MRI (ASL-MRI) using human calf-muscle and brain (Durduran 2004, Durduran et al. 2004b, 2007, 2009a, Yu et al. 2007). For example, a contact optical probe (see Figure 10.5a) was placed on the calf-muscles of seven healthy subjects for concurrent measurements with ASL-MRI (Yu et al. 2007). The calf (with the optical probe) was then placed into the MRI knee coil (see Figure 10.7a). The optical probe in the MRI room was connected to the DCS instrument in the control room by long optical fibers through a port in a magnetic-field-shielded wall. After a period of baseline, a large leg cuff on the thigh was inflated rapidly to occlude BF to the lower leg for 5 min. The BF indices measured by DCS were compared to the absolute ASL-MRI flow around the peak of the hyperemia after cuff release (note: one limitation of this measurement was the reliability (actually, lack thereof) of ASL-MRI at low-baseline flow levels ($<10\text{ mL}/100\text{ g}/\text{min}$ [Petersen et al. 2006]), which, in turn, prevented accurate calculations of relative flow changes from MRI. A good correlation ($R^2>0.6$) was observed with both the relative (see Figure 10.7b) and absolute (see Figure 10.7c) flow indices from DCS and absolute ASL-MRI flow. These observations suggest that with further systematic calibration along with improved modeling, it may be feasible to estimate absolute BF values.

10.6 In Vivo Applications of DCS

As mentioned above, the utility of DCS technology for monitoring tissue BF has been demonstrated in tumors (Menon et al. 2003, Wang et al. 2004, Durduran et al. 2005, Yu et al. 2005b, 2006, Sunar et al. 2006), brain (Culver et al. 2003a, c, Durduran 2004, Zhou et al. 2006), and skeletal muscles (Yu et al. 2005a, 2007). The early stages of many of these studies focused on BF in animal models (e.g., murine tumors (Yu et al. 2005b), rat and piglet brain (Cheung et al. 2001, Culver et al. 2003a, Zhou et al. 2006, 2009), and pig limb muscles (Xing et al. 2007). More recently, the DCS technique has been a key component in a variety of clinical studies (e.g., human cancers of prostate, breast and head and neck, cerebral functional activities, cerebral stroke, traumatic brain injury (TBI), and skeletal muscle physiology). In these preclinical and clinical investigations, DCS was used for quantification of tissue hemodynamic status, for diagnosis of disease, and for continuous monitoring and evaluation of therapeutic effects. The optical techniques were often validated as part of these measurements, e.g., by comparison to other diagnostic modalities (see Section 10.5). In total, the research demonstrated the utility of the DCS method and the range of its capabilities. Selected applications in cancer, brain, and muscle are given below.

10.6.1 Cancer Therapy Monitoring

DCS has been utilized to monitor tumor contrast in breast cancer (Durduran et al. 2005, Zhou et al. 2007), to monitor early physiological changes in breast cancer in response to chemotherapy (Zhou et al. 2007), to monitor the effects of chemoradiation therapy on head-and-neck cancer (Sunar et al. 2006), to monitor response to photodynamic therapy (PDT) in prostate cancer (Du et al. 2006, Yu et al. 2006), and to assess the efficacy of cancer therapy in murine tumor models (Menon et al. 2003, Yu et al. 2005b, Song et al. 2007, Sunar et al. 2007, Busch et al. 2009, Cerniglia et al. 2009). Measurement and assessment of tissue/tumor hemodynamic changes during cancer treatment is particularly attractive for cancer therapies

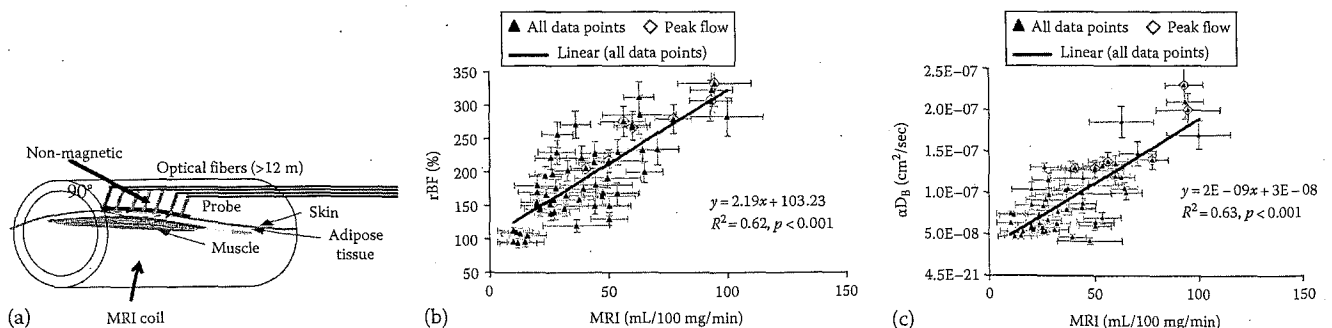


FIGURE 10.7 (a) Configuration of concurrent optical-MRI measurement. (b) Correlation between peak MRI flow and relative peak DCS flow. (c) Correlation of peak MRI flow and peak absolute DCS flow-index αD_b . Error bars were estimated from measurement repeatability. (From Yu, G. et al., *Opt. Express*, 15, 1064, 2007. With permission.)

that require tissue oxygen for treatment efficacy. For example, PDT requires tissue oxygen because the process creates singlet oxygen, which, in turn, kills tumor cells, and damages local vasculature (Yu et al. 2005b). PDT is well known to be less efficacious in patients with hypoxic tumors (Busch et al. 2000, Leach et al. 2002). Factors that modulate tissue oxygen include BF, blood oxygenation, and oxygen metabolism, i.e., factors that these new measurement tools can probe. Furthermore, cancer therapy can alter tumor hemodynamic/metabolic status, which further impacts treatment outcome. It is thus anticipated that functional assessment of tumor hemodynamic status during cancer therapy may provide information useful for early prediction of long-term treatment outcomes, thus enabling clinicians to optimize and individualize treatment. Tumor hemodynamics, however, are not routinely measured during cancer therapy due, in part, to a paucity of appropriate technologies.

In this subsection, we first describe a preclinical example that demonstrates the use of DCS for real-time monitoring of BF responses to PDT in murine tumors. A strong correlation between tumor hemodynamic changes during treatment and long-term treatment efficacy was found in this study, indicative of the clinical dosimetry potential of DCS for prediction of cancer therapy efficacy. A clinical translational study using DCS for monitoring and evaluation of prostate cancer therapy in humans is then described.

10.6.1.1 Prediction of Photodynamic Therapy in Murine Tumors

PDT requires administration of a photosensitizer that localizes in tumor tissue and is subsequently activated by exposure to optical radiation (Dougherty et al. 1998). The photoexcited photosensitizer initiates a cascade of chemical reactions, involving highly reactive oxygen intermediates that can cause necrosis and apoptosis of cells. Many studies suggest that PDT-mediated vascular damage significantly affects tissue oxygen

supply (BF) and thus contributes to long-term tumor response to therapy.

Monitoring of tumor hemodynamic responses during PDT, however, has proven difficult due to interference between measurement and treatment. In this study, a noncontact probe with source and detector fibers on the back image-plane of a camera was employed to avoid blocking the treatment light (see Figure 10.8a) (Yu et al. 2005b). Source-detector separations ranged from 1 to 4 mm, permitting light to penetrate to depths of ~ 0.5 – 2 mm below tumor surface. An optical filter mounted in front of the camera lens attenuated treatment light. DCS and the noncontact probe were employed to monitor the BF of murine tumors ($n=15$) during light illumination in Photofrin-mediated PDT. Measurements were also made at specific time points after treatment (Yu et al. 2005b).

Figure 10.8b shows relative changes of tumor BF (rBF) during PDT. Within minutes of the start of PDT, rBF rapidly increased, followed by a decline, and subsequent peaks and declines with variable kinetics. The experiments discovered that the slope (flow-reduction rate) and duration (interval time, data not shown) over which rBF decreased following the initial PDT-induced increase was highly associated with treatment durability (see Figure 10.8c); here, treatment durability was defined as the time of tumor growth to a volume of 400 mm^3 (pretreatment tumor volume was $\sim 100 \text{ mm}^3$). These findings were consistent with the hypothesis that treatment efficacy is a function of tumor oxygenation during PDT; under oxygen-limited conditions (e.g., such as might arise with rapidly declining BF), treatment efficacy was abrogated. After PDT, all animals showed decreases in rBF at 3 and 6 h, and rBF, at these time points, was also predictive of tumor response (data not shown) (Yu et al. 2005b).

Thus, these data demonstrate that DCS-measured changes in tumor rBF during and after Photofrin-PDT are predictive of treatment efficacy. The data further suggest that in situ BF monitoring during therapy may be very useful for real-time adjustment and optimization of PDT in humans.

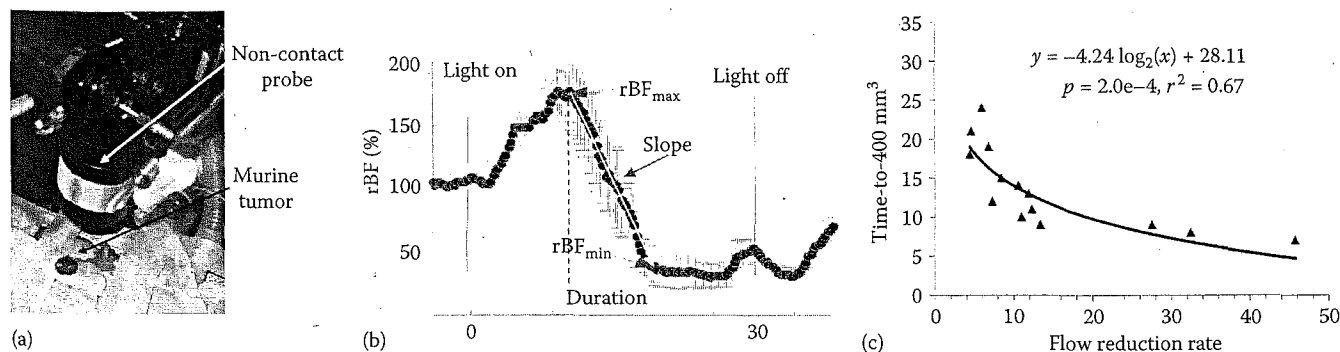


FIGURE 10.8 (a) Photograph of the noncontact DCS preclinical model probe. (b) Representative murine tumor BF responses to PDT. Plot shows rBF versus time (before, during, and just after PDT). Points with error bars represent the average \pm SD. rBF_{max} and rBF_{min} depict the maximum and minimum, respectively, of the first peak in BF. Notice the substantial fluctuations in relative BF during PDT. Flow-reduction rate is defined by the slope of the decrease in BF after its initial PDT-induced increase. (c) Correlation between treatment durability/efficacy (i.e., tumor time-to- 400 mm^3) and flow-reduction rate (slope). The results indicate that tumor rBF during Photofrin-PDT is predictive of treatment efficacy. (From Yu, G. et al., *Clin. Cancer Res.*, 11, 3543, 2005b.)

10.6.1.2 Real-Time *In Situ* Monitoring of Human Prostate PDT

Armed with promising results from the murine models above, Yu et al. (2006) proceeded to adapt the DCS system for use in a Phase I clinical trial of interstitial human prostate PDT. A thin side-illumination fiber-optic probe (see Figure 10.9a) containing source and detector fibers was constructed with multiple source-detector separations (0.5–1.5 cm) (Yu et al. 2006). The fiber-optic probe was placed inside an 18-gauge catheter that had already been inserted into the patient's prostate gland. Five patients with locally recurrent prostate cancer in the Phase I trial of motexafin lutetium (MLu)-mediated PDT were measured using DCS and the side-illumination probe. The prostate was illuminated sequentially in several quadrants (Q1 – Q4) until the entire gland was treated.

Measured BF variation showed a similar trend in each individual. Figure 10.9b and c shows typical responses in BF over the course of PDT in two prostatic tumors. As was the case for

murine tumors, a sharp decrease in prostate BF was observed [$-41 \pm 12\%$ ($n=5$)], suggesting that MLu-mediated PDT has an antivascular effect. The slope (flow-reduction rate) during PDT showed large interprostate heterogeneities; 15 %/min in Figure 10.9b versus 10 %/min in Figure 10.9c measured from two prostates during PDT. On average ($n=5$), the flow-reduction rate from the five subjects was 12 ± 5 (%/min).

Although, in this case, the study did not attempt to correlate clinical outcome with DCS-measured flow response during PDT, clearly PDT-induced flow responses hold potential for prediction of treatment outcomes in humans, as shown in murine tumor models. The present study took a step in this direction.

10.6.2 Cerebral Physiology and Disease

Noninvasive CBF measurements provide physiological insight critical for both preclinical models and in clinical applications.

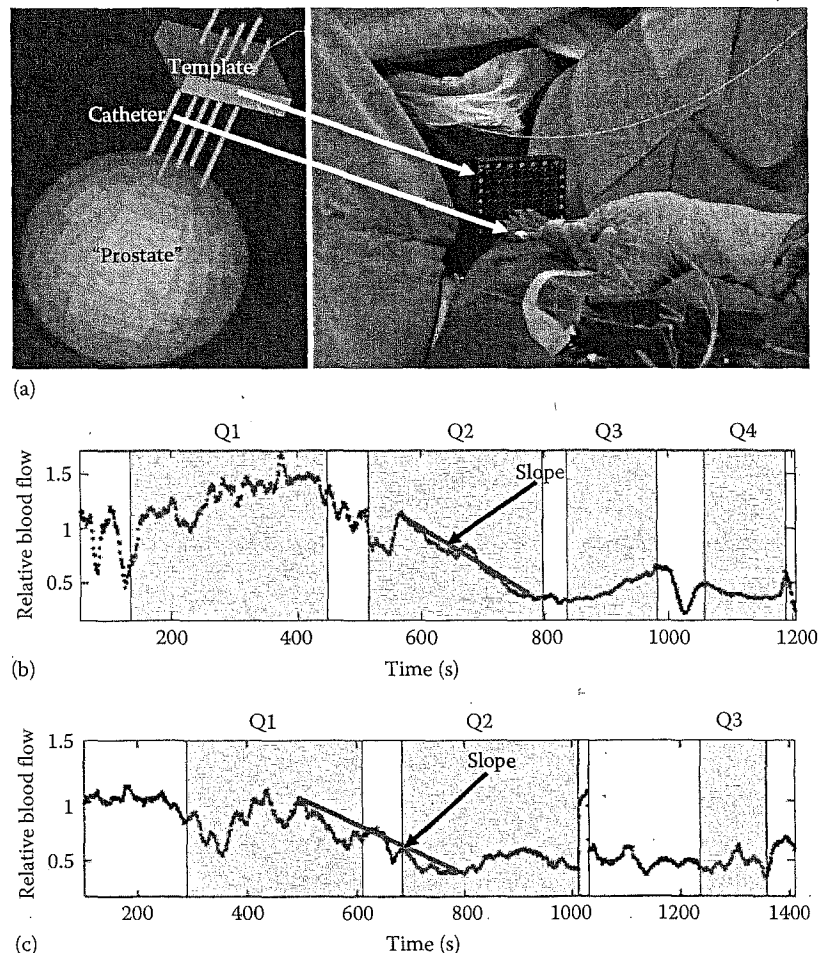


FIGURE 10.9 (a) Custom-made template for guidance of placing catheters for prostate PDT. The 732-nm treatment light was administered through the cylindrical diffusing fibers inside the catheters. Our small side-illumination probe was placed in the center of the prostate before PDT through one of the catheters. The catheter remained in place throughout PDT. (b) and (c) Tumor BF responses during PDT as a function of time measured from two prostates. Four quadrants of the prostate (Q1 – Q4) were illuminated sequentially until the entire gland was treated. The illumination periods are presented as shaded areas. Flow-reduction rate is defined by the slope of the decrease in BF. (From Yu, G. et al., *Photochem. Photobiol.*, 82, 1279, 2006. With permission.)

DCS was first utilized in rat brain models in a monitoring capacity (Cheung et al. 2001) and for demonstration of 3D DCS tomography (Culver et al. 2003a,b, Zhou et al. 2006). It has also been utilized in neonatal piglet models of head trauma, illustrating potential for continuous long-term "bedside" monitoring (Zhou et al. 2009). In 2004, its use in human brain (through intact skull) was first demonstrated (Durduran 2004), and subsequently, the techniques have been applied for functional studies of CBF in healthy adults (Durduran et al. 2004b, Li et al. 2005, 2008). Noteworthy comparative studies demonstrated that hemodynamic responses to external functional stimuli of the sensorimotor cortex were in line with ASL-MRI and fMRI studies. In the clinical settings, DCS use has been reported in premature infants (Buckley et al. 2009, Roche-Labarbe et al. 2010), in neonates with congenital heart defects (Durduran et al. 2010a), in adults with acute ischemic stroke (Durduran et al. 2009b), and in TBI patients (Kim et al. 2010). In this subsection, we describe several preclinical and clinical examples of the use of DCS for CBF measurement.

10.6.2.1 3D rCBF Tomography of Cortical Spreading Depression in Rat Brain

Zhou et al. (2006) demonstrated the feasibility of *in vivo* 3D tomographic reconstruction of relative cerebral blood flow (rCBF) using DCS to probe a rat brain cortical spreading depression (CSD) model (see Figure 10.10a). CSD is a wave of excitation and depolarization of neuronal cells that spreads radially with a speed of 2–5 mm/min over the cerebral cortex (Leao 1944). CSD is accompanied by robust and localized (on the cortex) BF changes (Nielsen 2000, Ayata 2004). Thus, CSD is a good model for testing the feasibility of 3D diffuse optical tomography of BF.

Figure 10.10b shows reconstructed rCBF images localized at the cortex layer of the rat brain (~1 mm deep) during CSD. In this case, CSD was induced by placing a 1-mm³ filter paper soaked in 2 mol/L potassium chloride (KCl) onto the dura. Images (a), from left to right, from top to bottom) are shown roughly every 20 s from immediately before KCl was applied ($t \approx 26$ s) until the end of the second CSD peak. Notice that a strong increase in BF appears from the top of the image and proceeds to the bottom of the image. After the first peak, a sustained decrease in BF is observed (~3 min), which covers most of the image area. Three regions of interest (ROI) were selected, and rCBF changes therein are plotted in Figure 10.10b. The propagation of the CSD waves can be clearly identified from the delay between each curve. Figure 10.10c shows the dependence of maximal rCBF changes on depth using the data from the second ROI-2 in Figure 10.10a. The maximal change occurs at 1 mm (i.e., just below the skull), corresponding to the cortex surface. The peak spreads ~0.5 mm above and below the cortical surface as expected from the "resolution" broadening of the diffuse photons. No significant change is observed at the surface ($z=0$ mm) nor in the deep region ($z=3$ mm). Clearly, three-dimensional tomographic *in vivo* relative BF information is revealed. A movie demonstrating rCBF changes at different

brain layers during CSD accompanies the original publication in *Optics Express* (Zhou et al. 2006).

10.6.2.2 Cerebral Cortical Blood Flow Responses to Functional Activity

The first reported use of DCS in human brain probed local CBF with DCS in motor cortex during sensorimotor stimuli (Durduran et al. 2004b). Durduran et al. (2004b) and later Gisler and coworkers (Li et al. 2005) reported measurements of cortical BF to finger-tapping stimulation. Importantly, Durduran et al. employed a hybrid optical instrument that combined DCS with NIRS to measure CBF as well as the concentrations of oxygenated hemoglobin (HbO₂), deoxygenated hemoglobin (Hb), and THC. They then combined this information in a model for cerebral metabolic rate of oxygen consumption (CMRO₂) to derive the variations of CMRO₂ during sensorimotor activation by an *all-optical* method. CMRO₂, in particular, is of great interest to the neuroscientists. The population-averaged results exhibited a robust change, which correlated with the activation. Mean changes observed were $39 \pm 10\%$ for rCBF, $12.5 \pm 2.8 \mu\text{M}$ for HbO₂, $-3.8 \pm 0.8 \mu\text{M}$ for Hb, $8.3 \pm 2.3 \mu\text{M}$ for THC, and $10.1\% \pm 4.4\%$ for rCMRO₂. The CBF changes measured were well within the literature values (Roland et al. 1980, Colebatch et al. 1991, Seitz and Roland 1992, Ye et al. 1999, Kastrup et al. 2002). NIRS results were harder to cross-validate, since similar data are not available from other modalities. However, the NIRS results were in qualitative agreement with BOLD-fMRI (Kastrup et al. 2002, Mehagnoul-Schipper et al. 2002). Most interestingly, the increase in CMRO₂ is also within the range of values from hybrid MRI measurements (Hoge et al. 1999, Kastrup et al. 2002). Similar results have been recently reported in visual stimuli as well (Li et al. 2008).

10.6.2.3 CMRO₂ Estimates by NIRS-Only and NIRS-DCS in Premature Infants

In Section 10.5.1, experiments by Roche-Labarbe et al. (2010) were described; these measurements utilized DCS in premature born infants and validated its use against TCD (ultrasound) measurements. In the same report, the authors also demonstrate that the combination of NIRS and DCS to derive CMRO₂ could be more robust than NIRS-only models that they had utilized previously. They obtained measurements at multiple positions on the head and on a weekly basis for the first 6 weeks of life as shown in Figure 10.11. Interestingly, the THC concentration and the blood oxygen-saturation decrease as the premature born infant matures over time. This is in contrast to increasing CBF measured by DCS. If THC concentration is converted to cerebral blood volume (CBV) utilizing a simple model, there is no trend in CBV over time. Furthermore, if CBV is then utilized to derive CMRO₂ as is done in NIRS-only approaches, then both CBV and CMRO₂ appear unaltered over time. On the other hand, if CMRO₂ is derived using NIRS-DCS hybrid data, a linear increase with time is observed. This is in qualitative agreement with physiological expectations, which dictate that blood oxygen-saturation should decrease while

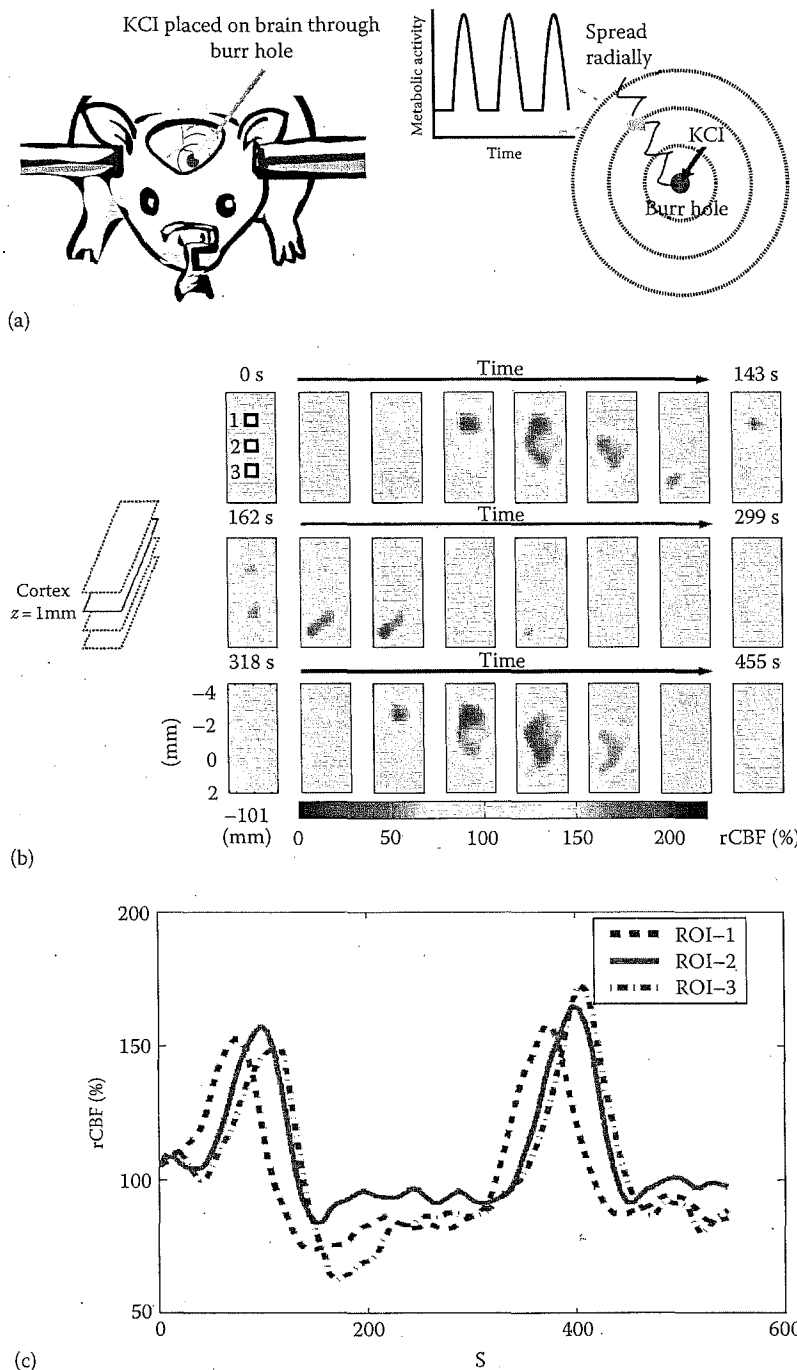


FIGURE 10.10 (See color insert.) CSD in rat brain. (a) A rat was fixed on a stereotaxic frame with the scalp retracted and the skull intact. CSD was induced by placing KCl solution on the rat brain through a small hole drilled through the skull. Periodic activations and deactivations of the neurons then spread out radially on the cortex. (b) rCBF changes on the cortex of the rat brain (~1 mm deep) as a function of time during CSD. rCBF images from the cortex (from left to right, from top to bottom) are shown roughly every 20 s starting immediately before KCl was applied until the end of the second CSD peak. A strong increase in BF appears from the top and proceeds to the bottom of the image. After the peak, there is a sustained decrease in BF, which covers most of the image area. The amount of rCBF changes is reflected in the image as a spectrum of color, with deep blue indicates a decrease in rCBF and dark red indicates an increase in rCBF. (c) Temporal rCBF curves from three ROI indicated in the 0 s image in (b), demonstrating the propagation of the CSD waves. (From Zhou, C. et al., *Opt. Express*, 14, 1125, 2006. With permission.)

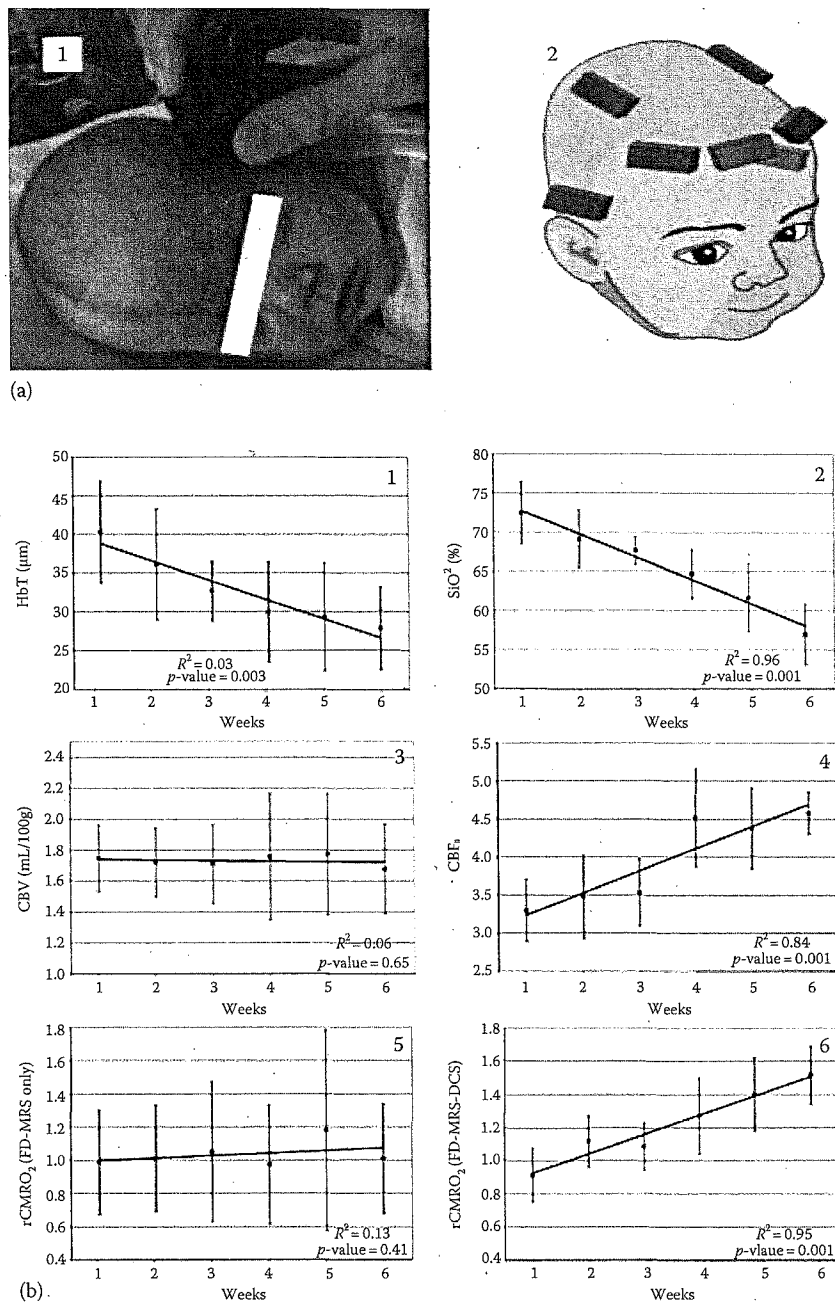


FIGURE 10.11 (a1) Picture schematic of a subject during measurement. (a2) Locations of recording on the subject's head. (b) Averages \pm 95% confidence intervals as a function of age. (b1) THC concentration (HbT). (b2) Microvascular blood StO_2 . (b3) CBV. (b4) Cerebral BF index (CBFix). (b5) $rCMRO_2$ estimated from FD-NIRS only. (b6) $rCMRO_2$ calculated by combining FD-NIRS and DCS. Bold lines are linear regressions; R^2 and P -value of the regressions are in the bottom right corner of each graph. HbT and StO_2 decrease while CBF increases as the premature born infant matures over time. When HbT is converted to CBV, the trends vanish and therefore if NIRS alone is used to derive $CMRO_2$, there are no trends in $CMRO_2$. However, if $CMRO_2$ is derived using NIRS-DCS hybrid data, a linear increase with time is observed. (From Roche-Labarbe, N. et al., *Hum. Brain Mapp.*, 31(3), 341, 2010. With permission.)

CBF is increasing; that is, oxygen utilization as well as oxygen metabolism should be increasing with the infant's age. The authors argue that these findings demonstrate the robustness of the NIRS-DCS combined model (notice large error bars in subfigure (5)), which might be expected since this model relies on fewer approximations than the NIRS-only model (Boas et al.

2003). Taken together with other recent reports (Durduran et al. 2010a) of DCS-NIRS use in neonates to estimate $CMRO_2$, current research demonstrates the feasibility and the importance of concurrent DCS and NIRS; the two complementary methodologies permit measurement of microvascular hemodynamics in a previously inaccessible way.

10.6.2.4 Cerebrovascular Hemodynamics in Adult Neurointensive Care Units

Working closely with neurologists, optical scientists have identified an unfilled niche application for DCS–NIRS hybrid approach as a bedside monitor in neurointensive care units for adults. To this end, we have studied the responses of a cohort of acute ischemic stroke patients (Durduran et al. 2009b) and TBI patients (Kim et al. 2010). In TBI patients, we have validated DCS against portable xenon-CT (Kim et al. 2008) and demonstrated good agreement with invasive measurements of intracranial pressure, cerebral perfusion pressure, and the partial pressure of oxygen during postural changes and hyperoxia. Here, we highlight our findings in acute ischemic stroke patients.

In the acute ischemic stroke population, we have induced mild orthostatic stress by changes in head-of-bed (HOB) positioning as shown in Figure 10.12a, with probes placed on the forehead near the frontal poles. CBF and hemoglobin concentrations were measured sequentially for 5 min at each HOB positions: 30, 15, 0, -5, and 0 degrees and normalized to their values at 30 degrees. In Figure 10.12b (left), the infarcted hemisphere (peri-infarct) shows a very large CBF increase in response to lowering of HOB position, whereas the opposite hemisphere (contra-infarct) shows minimal changes that are similar to those observed on healthy people. While this was expected and observed in most (~75%) of the people ($n=17$), others have shown a “paradoxical” response

(see Figure 10.12b, right) where CBF decreased in response to lowering of the HOB position. Larger changes in peri-infarct hemisphere are presumably due to damaged cerebral autoregulation and are observed in both types of responses. The existence of the paradoxical response is an indicator for the potential usefulness of a bedside monitor for individualized stroke care. In control populations (Durduran et al. 2009b, Edlow et al. 2010), we have shown that both hemispheres behave in an identical fashion with postural challenge, as expected. Among other things, the example illustrates that diffuse optical instrumentation can be deployed at the neurointensive unit to directly monitor injured tissues.

10.6.3 Skeletal Muscle Hemodynamics

Characterization of the oxygen supply and metabolism with optical methods in skeletal muscles has important implications in exercise medicine, and for treatment, screening, and understanding of diseases such as the PAD. In addition, these types of measurements hold potential to improve fundamental understanding of muscle function within the context of the cardiovascular disease (Cheatle et al. 1991, Wallace et al. 1999).

In a pilot study (Yu et al. 2005a), issues of light penetration and flow sensitivity were addressed by experimentally investigating tissue layer responses during prolonged cuff occlusion.

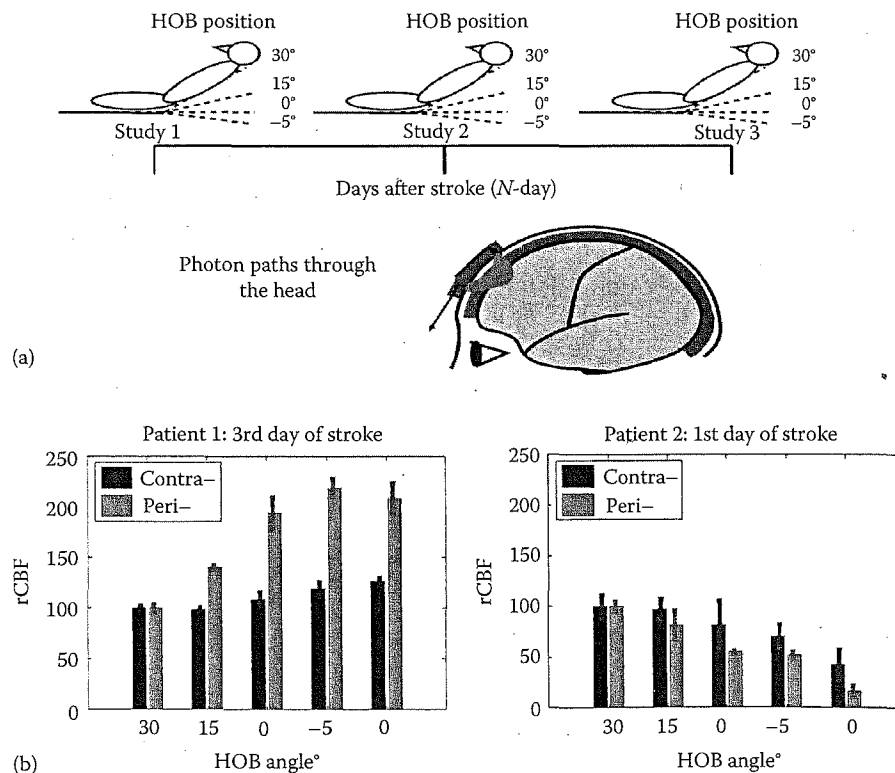


FIGURE 10.12 (a) Illustration of the measurement protocol and the probe positioning. (b) CBF data taken over 25 min from two representative subjects. A representative plot (left) was observed in about 75% of the subjects ($n=17$); the infarcted hemisphere (peri-infarct) shows a very large CBF increase in response to lowering of HOB position. Others have shown a “paradoxical” response (right) where CBF decreased in response to lowering of the HOB position. (From Durduran, T. et al., *Opt. Express*, 17, 3884, 2009b. With permission.)

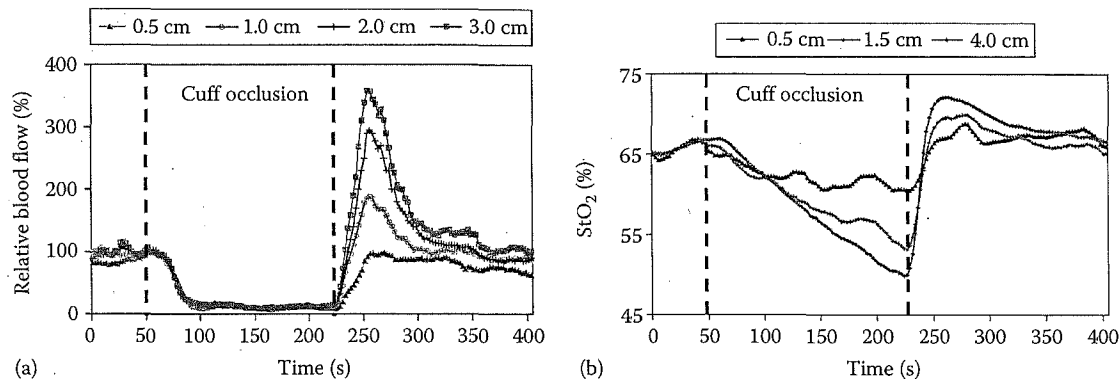


FIGURE 10.13 Representative curves of relative BF (a) and tissue blood oxygen saturation (StO_2) (b) as function of time during arterial cuff occlusion. Data are shown from different source-detector pairs measured on a healthy leg. The source-detector separations in the figure are 0.5, 1, 2, and 3 cm for DCS flow measurement and 0.5, 1.5, and 4.0 cm for NIRS oxygenation measurement, respectively. Vertical lines indicate the beginning and end of the occlusion period. Stronger reactive hyperemia after the release of occlusion and deoxygenation during occlusion were derived from source-detector pairs with large separations, i.e., 2 and 3 cm for DCS and 1.5 and 4 cm for NIRS, respectively. (From Yu, G. et al., *J. Biomed. Opt.*, 10, 024027, 2005a. With permission.)

A contact fiber-optical probe with source-detector separations of 0.5, 1, 2, and 3 cm was employed for this study (see Figure 10.5a). Based on diffusion theory, the light penetration depth depends on tissue optical properties and source-detector separation (typically, penetration is approximately one-third to one-half of the source-detector separation on the tissue surface).

Ten healthy subjects and one patient with PAD were measured. A 3 min cuff occlusion protocol was used to investigate the different layer responses in skeletal muscles in order to estimate light penetration depth and to validate results in the ischemic states. A skinfold caliper was used to mechanically measure the thickness of the upper layers (skin and adipose) above muscle. The thickness of the upper layers (skin and adipose tissues) above leg flexors and wrist flexors was 5.5 ± 0.4 mm and 2.8 ± 0.6 mm, respectively ($n=10$). Therefore, the optical signals detected from the large separations (≥ 2 cm) are mainly from the deep muscle tissues.

Figure 10.13 shows the typical responses of rBF and blood O_2 saturation (StO_2) during leg arterial occlusion from the different source-detector pairs on a healthy individual. Hemodynamic responses derived from source-detector pairs with large separations (≥ 2 cm) were significantly stronger than those from the shortest source-detector separations (0.5 cm), consistent with the larger responses expected for muscle tissue compared to top skin and adipose tissues.

Table 10.1 lists the hemodynamic responses in cuff occlusions from 10 healthy volunteers and one PAD patient. For the healthy volunteers, cuff occlusion of the leg flexor and arm flexor muscles produced a similar response. The hemodynamic response trends in the PAD patient (data not shown) were similar to those of the healthy volunteers, and different responses were not found in the arm muscles of healthy controls compared to the patient. However, in the PAD patient leg muscle, the relative magnitude of reactive hyperemia was $\sim 1/2\times$ of the controls, and the

recovery half-time of both StO_2 and rBF after occlusion was $\sim 3\times$ those of the controls.

Further investigations will test the capability of diffuse optical techniques for screening and diagnosis of PAD. In a different vein, the community has begun to consider DCS measurement during exercise, but these measurements can have motional artifacts; better understanding and characterization of these motional artifacts is needed and may require analysis of the methodologies at a fundamental level.

10.7 Summary

In this chapter, we have outlined the development and application of DCS. The technique has now been adopted by several research groups around the world for measurement of BF in deep tissues. In a relatively short time, we have witnessed the translation of DCS from its theoretical conception to its application in intensive care units at the hospital. These diffuse optical methods are flexible, portable, and rapid and can be combined with other modalities such as NIRS or tomography, MRI, PET, and CT. Currently, its use is limited to measurements of relative BF, but promising results are indicative of potential for absolute measurements in the future.

Open questions about the technique still remain and will be interesting to consider. For example, the interaction of photons with moving red-blood cells in the complex environment of the tissue microvasculature is only partially understood (see Section 10.3.3). Thus, empirical approaches to defining BF indices have been adopted. While these empirical indices have withstood extensive cross-validation (see Section 10.5), it remains desirable to generate a more fundamental understanding of the origins of this BF index. We expect improved physical understanding, along with many more clinical applications, to emerge rapidly as the technique is adopted by others.

TABLE 10.1 Responses in Cuff Occlusions from 10 Healthy Volunteers and 1 PAD Patient

Parameters	Subjects	T_m (s)	Max Δ	T_{50} (s)	OS (Δ)
Leg Occlusion					
StO ₂ (%)	Healthy	177.1 ± 20.7	-16.4 ± 4.4	33.7 ± 26.0	3.8 ± 1.7
	PAD	180.0	-15.0	96.0*	3.0
THC (μM)	Healthy	88.1 ± 81.9	-1.8 ± 5.9	16.2 ± 18.3	2.8 ± 3.1
	PAD	25.0	-10.0	36.0	5.0
rBF (%)	Healthy	51.0 ± 11.5	-90.0 ± 2.4	25.6 ± 14.5	311.4 ± 90.8
	PAD	60.0	-93.0	90.0*	165.0*
Arm Occlusion					
StO ₂ (%)	Healthy	174.7 ± 15.3	-25.1 ± 8.2	19.4 ± 15.2	11.4 ± 5.0
	PAD	180.0	-23.0	23.0	10.0
THC (μM)	Healthy	46.6 ± 61.2	-1.4 ± 6.4	13.6 ± 7.3	8.6 ± 5.0
	PAD	111.0	-16.0	20.0	22.0
rBF (%)	Healthy	14.0 ± 7.4	-90.3 ± 3.8	11.3 ± 6.1	445.1 ± 194.1
	PAD	11.0	-92.0	12.0	450.0

Source: Yu, G. et al., *J. Biomed. Opt.*, 10, 024027, 2005a, Table 1. With permission.

Time to reach maximal change (T_m), maximal change (Max Δ), recovery half-time (T_{50}), and hyperemic overshoot (OS) are shown for StO₂ (%), THC (μM), and rBF (%). The 100% is assigned for baseline BF. Means ± SD are reported.

*Substantially different, healthy volunteers versus the PAD patient.

Acknowledgments

We gratefully acknowledge collaborations and discussions with numerous scientists at the University of Pennsylvania and in the biomedical optics community in general. Our work would not have been possible without the support and guidance of our clinical and physiological collaborators. Much of the research described in this review was facilitated by collaborations over many years with many colleagues, including David Boas, Erin Buckley, Theresa Busch, Britton Chance, Cecil Cheung, Joseph Culver, Regine Choe, John Detre, Lixin Dong, Douglas Fraker, Thomas Floyd, Joel Greenberg, Steven Hahn, Andrew Kofke, Meeri Kim, Daniel Licht, Gwen Lech, Emilie Mohler, Susan Margulies, Goro Nishimura, Harry Quon, Mark Rosen, Mitchell Schnall, Ulas Sunar, Bruce Tromberg, Jionjong Wang, Xiaoman Xing, and Leonid Zubkov. One of us (AGY) particularly acknowledges the collaboration and camaraderie of Britton Chance, who for two-decades provided us with his institution encouragement, and willing ear.

Grant Acknowledgments

We gratefully acknowledge support from

- **NIH grants:** CA-149274 (G. Yu), HL-083225, HL-57835 (A. G. Yodh), NS-60653 (A. G. Yodh), RR-02305 (A. G. Yodh and R. Reddy), EB-07610 (T. Durduran), Ns-45839 (A. G. Yodh), CA-126187 (A. G. Yodh)
- **AHA grants:** BGIA 2350015 (G. Yu), BGIA 0665446U (G. Yu)

- **DOD award:** W81XWH-04-1-0006 (G. Yu)
- **Thrasher Research Fund:** NR 0016 (T. Durduran)
- **Fundacio Cellex Barcelona** (T. Durduran)

References

- Ackerson, B. J., Dougherty, R. L., Reguigui, N. M., and Nobbman, U. 1992. Correlation transfer: Application of radiative transfer solution methods to photon correlation problems. *J. Thermophys. Heat Trans.* 6: 577–588.
- Ackerson, B. J. and Pusey, P. N. 1988. Shear-induced order in suspensions of hard-spheres. *Phys. Rev. Lett.* 61: 1033–1036.
- Ayata, C., Shin, H. K., Salomone, S. et al. 2004. Pronounced hypoperfusion during spreading depression in mouse cortex. *J. Cereb. Blood Flow Metab.* 24(10): 1172–1182.
- Baron, J. C. 1999. Mapping the ischaemic penumbra with PET: Implications for acute stroke treatment. *Cerebrovasc. Dis.* 9: 193–201.
- Belau, M., Ninck, M., Hering, G. et al. 2010. Noninvasive observation of skeletal muscle contraction using near-infrared time-resolved reflectance and diffusing-wave spectroscopy. *J. Biomed. Opt.* 15: 057007.
- Benaron, D. A. and Stevenson, D. K. 1993. Optical time-of-flight and absorbance imaging of biologic media. *Science* 259: 1463–1466.
- Berne, B. J. and Pecora, R. 1990. *Dynamic Light Scattering with Applications to Chemistry, Biology, and Physics*. Malabar, FL: Krieger.
- Binzoni, T., Leung, T. S., Seghier, M. L., and Delpy, D. T. 2004. Translational and Brownian motion in laser-Doppler flowmetry of large tissue volumes. *Phys. Med. Biol.* 49: 5445–5458.

- Boas, D. 1996. Diffuse photon probes of structural and dynamical properties of turbid media: Theory and biomedical applications. PhD dissertation, University of Pennsylvania, Philadelphia, PA.
- Boas, D. A., Campbell, L. E., and Yodh, A. G. 1995. Scattering and imaging with diffusing temporal field correlations. *Phys. Rev. Lett.* 75: 1855–1858.
- Boas, D. A., Culver, J. P., Stott, J. J., and Dunn, A. K. 2002. Three dimensional Monte Carlo code for photon migration through complex heterogeneous media including the adult human head. *Opt. Express* 10: 159–170.
- Boas, D. A., Strangman, G., Culver, J. P. et al. 2003. Can the cerebral metabolic rate of oxygen be estimated with near-infrared spectroscopy? *Phys. Med. Biol.* 48: 2405–2418.
- Boas, D. A. and Yodh, A. G. 1997. Spatially varying dynamical properties of turbid media probed with diffusing temporal light correlation. *J. Opt. Soc. Am. A Opt. Image Sci. Vis.* 14: 192–215.
- Bonner, R. and Nossal, R. 1981. Model for laser Doppler measurements of blood flow in tissue. *Appl. Opt.* 20: 2097–2107.
- Bonner, R. F., Nossal, R., Havlin, S., and Weiss, G. H. 1987. Model for photon migration in turbid biological media. *J. Opt. Soc. Am. A* 4: 423–432.
- Briers, J. D. 2001. Laser Doppler, speckle and related techniques for blood perfusion mapping and imaging. *Physiol. Meas.* 22: R35–R66.
- Brown, W. 1993. *Dynamic Light Scattering: The Method and Some Applications*. New York: Clarendon Press.
- Buckley, E. M., Cook, N. M., Durduran, T. et al. 2009. Cerebral hemodynamics in preterm infants during positional intervention measured with diffuse correlation spectroscopy and transcranial Doppler ultrasound. *Opt. Express* 17: 12571–12581.
- Busch, T. M., Hahn, S. M., Evans, S. M., and Koch, C. J. 2000. Depletion of tumor oxygenation during photodynamic therapy: Detection by the hypoxia marker EF3 [2-(2-nitroimidazol-1-[H]-yl)-N-(3,3,3-trifluoropropyl)acetamide]. *Cancer Res.* 60: 2636–2642.
- Busch, T. M., Xing, X., Yu, G. et al. 2009. Fluence rate-dependent intratumor heterogeneity in physiologic and cytotoxic responses to Photofrin photodynamic therapy. *Photochem. Photobiol. Sci.* 8: 1683–1693.
- Carp, S. A., Dai, G. P., Boad, D. A. et al. 2010. Validation of diffuse correlation spectroscopy measurements of rodent cerebral blood flow with simultaneous arterial spin labeling MRI: towards MRI-optical continuous cerebral metabolic monitoring. *Biomed. Opt. Express* 1(2): 553–565.
- Cerniglia, G. J., Pore, N., Tsai, J. H. et al. 2009. Epidermal growth factor receptor inhibition modulates the microenvironment by vascular normalization to improve chemotherapy and radiotherapy efficacy. *PLoS One* 4: e6539.
- Chance, B. 1998. Near-infrared images using continuous, phase-modulated, and pulsed light with quantitation of blood and blood oxygenation. *Adv. Opt. Biopsy Opt. Mammography Ann. NY Acad. Sci.* 838: 19–45.
- Chance, B., Anday, E., Nioka, S. et al. 1998. A novel method for fast imaging of brain function, non-invasively, with light. *Opt. Express* 2: 411–423.
- Cheatle, T. R., Potter, L. A., Cope, M. et al. 1991. Near-infrared spectroscopy in peripheral vascular disease. *Br. J. Surg.* 78: 405–408.
- Chen, Z., Milner, T. E., Wang, X., Srinivas, S., and Nelson, J. S. 1998. Optical Doppler tomography: Imaging in vivo blood flow dynamics following pharmacological intervention and photodynamic therapy. *Photochem. Photobiol.* 67: 56–60.
- Cheung, C., Culver, J. P., Takahashi, K., Greenberg, J. H., and Yodh, A. G. 2001. In vivo cerebrovascular measurement combining diffuse near-infrared absorption and correlation spectroscopies. *Phys. Med. Biol.* 46: 2053–2065.
- Cheung, R., Solonenko, M., Busch, T. M. et al. 2003. Correlation of in vivo photosensitizer fluorescence and photodynamic-therapy-induced depth of necrosis in a murine tumor model. *J. Biomed. Opt.* 8: 248–252.
- Choe, R., Konecky, S. D., Corlu, A. et al. 2009. Differentiation of benign and malignant breast tumors by in-vivo three-dimensional parallel-plate diffuse optical tomography. *J. Biomed. Opt.* 14: 024020.
- Chu, B. (ed.) (1991) *Laser Light Scattering: Basic Principles and Practice*. New York: Academic Press.
- Colebatch, J. G., Deiber, M. P., Passingham, R. E., Friston, K. J., and Frackowiak, R. S. J. 1991. Regional cerebral blood-flow during voluntary arm and hand movements in human subjects. *J. Neurophysiol.* 65: 1392–1401.
- Culver, J. P., Durduran, T., Furuya, T. et al. 2003a. Diffuse optical tomography of cerebral blood flow, oxygenation, and metabolism in rat during focal ischemia. *J. Cereb. Blood Flow Metab.* 23: 911–924.
- Culver, J. P., Siegel, A. M., Stott, J. J., and Boas, D. A. 2003b. Volumetric diffuse optical tomography of brain activity. *Opt. Lett.* 28: 2061–2063.
- Culver J. P., Durduran T., Cheung C., Furuya D., Greenberg J. H., and Yodh A. G. 2003c. Diffuse optical measurement of hemoglobin and cerebral blood flow in rat brain during hypercapnia, hypoxia and cardiac arrest. *Adv Exp Med Biol.* 510: 293–297.
- Detre, J. A., Leigh, J. S., Williams, D. S., and Koretsky, A. P. 1992. Perfusion imaging. *Magn. Reson. Med.* 23: 37–45.
- Dietsche, G., Ninck, M., Ortoft, C. et al. 2007. Fiber-based multispeckle detection for time-resolved diffusing-wave spectroscopy: Characterization and application to blood flow detection in deep tissue. *Appl. Opt.* 46: 8506–8514.
- Dougherty, T. J., Gomer, C. J., Henderson, B. W., Jori, G., Kessel, D., Korbelik, M., Moan, J., and Peng, Q. 1998. Photodynamic therapy. *J. Nat. Cancer Inst.* 90: 889–905.
- Du, K. L., Mick, R., Busch, T. et al. 2006. Preliminary results of interstitial motexafin lutetium-mediated PDT for prostate cancer. *Lasers Surg. Med.* 38: 427–434.
- Dunn, A. K., Bolay, T., Moskowitz, M. A., and Boas, D. A. 2001. Dynamic imaging of cerebral blood flow using laser speckle. *J. Cereb. Blood Flow Metab.* 21: 195–201.

- Durduran, T. 2004. Non-invasive measurements of tissue hemodynamics with hybrid diffuse optical methods. PhD thesis, University of Pennsylvania, Philadelphia, PA.
- Durduran, T., Burnett, M. G., Yu, G. et al. 2004a. Spatiotemporal quantification of cerebral blood flow during functional activation in rat somatosensory cortex using laser-speckle flowmetry. *J. Cereb. Blood Flow Metab.* 24: 518–525.
- Durduran, T., Choe, R., Culver, J. P. et al. 2002. Bulk optical properties of healthy female breast tissue. *Phys. Med. Biol.* 47: 2847–2861.
- Durduran, T., Choe, R., Yu, G. et al. 2005. Diffuse optical measurement of blood flow in breast tumors. *Opt. Lett.* 30: 2915–2917.
- Durduran, T., Kim, M. N., Buckley, E. M., et al. 2009a. Validation of diffuse correlation spectroscopy for measurement of cerebral blood flow across spatial scales and against multiple modalities. *SPIE Photonics West*. San Jose, CA, 2009, SPIE.
- Durduran, T., Kim, M. N., Buckley, E. M. et al. 2008. Diffuse optical monitoring of cerebral oxygen metabolism at the bedside in cerebrovascular disorders. *OSA: Annual Meeting, Frontiers in Optics*. Rochester, NY, 2008, OSA.
- Durduran, T., Yu, G., Burnett, M. G. et al. 2004b. Diffuse optical measurement of blood flow, blood oxygenation, and metabolism in a human brain during sensorimotor cortex activation. *Opt. Lett.* 29: 1766–1768.
- Durduran, T., Zhou, C., Buckley, E. M. et al. 2010a. Optical measurement of cerebral hemodynamics and oxygen metabolism in neonates with congenital heart defects. *J. Biomed. Opt.* 15(3): 037004.
- Durduran, T., Choe, R., Baker, W. B. et al. 2010b. Diffuse optics for tissue monitoring and tomography. *Rep. Prog. Phys.* 73(2010): 076701.
- Durduran, T., Zhou, C., Edlow, B. L. et al. 2009b. Transcranial optical monitoring of cerebrovascular hemodynamics in acute stroke patients. *Opt. Express* 17: 3884–3902.
- Durduran, T., Zhou, C., Yu, G. et al. 2007. Preoperative measurement of CO₂ reactivity and cerebral autoregulation in neonates with severe congenital heart defects. *SPIE Photonics West*. San Jose, CA, 2007, SPIE.
- Edlow, B. L., Kim, M. N., Durduran, T. et al. 2010. The effect of healthy aging on cerebral hemodynamic responses to posture change. *Physiol. Meas.*, 31(4):477–495.
- Einstein, A. 1905. On the motion of small particles suspended in liquids at rest required by the molecular-kinetic theory of heat. *Ann. Phys.* 17: 549–560.
- Fantini, S., Hueber, D., Franceschini, M. A. et al. 1999. Non-invasive optical monitoring of the newborn piglet brain using continuous-wave and frequency-domain spectroscopy. *Phys. Med. Biol.* 44: 1543–1563.
- Feke, G. T. and Riva, C. E. 1978. Laser Doppler measurements of blood velocity in human retinal-vessels. *J. Opt. Soc. Am.* 68: 526–531.
- Gagnon, L., Desjardins, M., Bherer, L., and Lesage, F. 2009. Double layer estimation of flow changes using diffuse correlation spectroscopy. *Optical Tomography and Spectroscopy of Tissue VIII*. San Jose, CA, 2009, Proc. SPIE.
- Gagnon, L., Desjardins, M., Jehanne-Lacasse, J., Bherer, L., and Lesage, F. 2008. Investigation of diffuse correlation spectroscopy in multi-layered media including the human head. *Opt. Express* 16: 15514–15530.
- Gisler, T., Ruger, H., Egelhaaf, S. U. et al. 1995. Mode-selective dynamic light scattering: theory versus experimental realization. *Appl. Opt.* 34: 3546–3553.
- Gisler, T., Rueger, H., Engelhaaf, S. U. et al. 1997. Mode-selective dynamic light scattering: theory versus experimental realization. *Appl. Opt. (Reprint)* 34: 3546–3553.
- Gopinath, S. P., Robertson, C. S., Grossman, R. G., and Chance, B. 1993. Near-infrared spectroscopic localization of intracranial hematomas. *J. Neurosurg.* 79: 43–47.
- Haskell, R. C., Svaasand, L. O., Tsay, T. et al. 1994. Boundary conditions for the diffusion equation in radiative transfer. *J. Opt. Soc. Am. A* 11: 2727–2741.
- Heckmeier, M., Skipetrov, S. E., Maret, G., and Maynard, R. 1997. Imaging of dynamic heterogeneities in multiple-scattering media. *J. Opt. Soc. Am.* 14: 185–191.
- Hielscher, A., Tittel, F. K., and Jacques, S. L. 1993. Non-invasive monitoring of blood oxygenation by phase resolved transmission spectroscopy. In: *Photon Migration and Imaging in Random Media and Tissues*, eds. B. Chance and R. R. Alfano. Los Angeles, CA: SPIE, pp. 275–288.
- Hoge, R. D., Atkinson, J., Gill, B. et al. 1999. Linear coupling between cerebral blood flow and oxygen consumption in activated human cortex. *Proc. Natl. Acad. Sci. U. S. A.* 96: 9403–9408.
- Hoskins, P. R. 1990. Measurement of arterial blood-flow by Doppler ultrasound. *Clin. Phys. Physiol. Meas.* 11: 1–26.
- Jacques, S. L. 1989. Time-resolved reflectance spectroscopy in turbid tissues. *IEEE Trans. Biomed. Eng.* 36: 1155–1161.
- Jaillon, F., Skipetrov, S. E., Li, J. et al. 2006. Diffusing-wave spectroscopy from head-like tissue phantoms: Influence of a non-scattering layer. *Opt. Express* 14: 10181–10194.
- Kastrup, A., Kruger, G., Neumann-Haefelin, T., Glover, G. H., and Moseley, M. E. 2002. Changes of cerebral blood flow, oxygenation, and oxidative metabolism during graded motor activation. *Neuroimage* 15: 74–82.
- Kidwell, C. S., Alger, J. R., and Saver, J. L. 2003. Beyond mismatch: Evolving paradigms in imaging the ischemic penumbra with multimodal magnetic resonance imaging. *Stroke* 34: 2729–2735.
- Kim, M. N., Durduran, T., Frangos, S. et al. 2008. Validation of diffuse correlation spectroscopy against xenon CTCBF in humans after traumatic brain injury or subarachnoid hemorrhage. *Neurocritical Care Society Annual Meeting*. Miami, FL, 2008.
- Kim, M. N., Durduran, T., Frangos, S. et al. 2010. Noninvasive measurement of cerebral blood flow and blood oxygenation using near-infrared and diffuse correlation spectroscopies in critically brain-injured adults. *Neurocrit. Care* 12(2): 173–180.
- Kuebler, W. M. 2008. How NIR is the future in blood flow monitoring? *J. Appl. Physiol.* 104: 905–906.

- Latchaw, R. E., Yonas, H., Hunter, G. J. et al. 2003. Guidelines and recommendations for perfusion imaging in cerebral ischemia: A scientific statement for healthcare professionals by the writing group on perfusion imaging, from the Council on Cardiovascular Radiology of the American Heart Association. *Stroke* 34: 1084–1104.
- Leach, R. M., Hill, H. S., Snetkov, V. A., and Ward, J. P. T. 2002. Hypoxia, energy state and pulmonary vasomotor tone. *Respir. Physiol. Neurobiol.* 132: 55–67.
- Leao, A. A. P. 1944. Spreading depression of activity in the cerebral cortex. *J. Neurophysiol.* 7: 359–390.
- Li, J., Dietsche, G., Iftime, D. et al. 2005. Noninvasive detection of functional brain activity with near-infrared diffusing-wave spectroscopy. *J. Biomed. Opt.* 10: 044002-1–044002-12.
- Li, J., Ninck, M., Koban, L. et al. 2008. Transient functional blood flow change in the human brain measured noninvasively by diffusing-wave spectroscopy. *Opt. Lett.* 33: 2233–2235.
- Li, Z., Krishnaswamy, V., Davis, S. C. et al. 2009. Video-rate near infrared tomography to image pulsatile absorption properties in thick tissue. *Opt. Express* 17: 12043–12056.
- Liu, D.L., Svanberg, K., Wang, I., Andersson-Engels, S., and Svanberg, S. 1997. Laser Doppler perfusion imaging: New technique for determination of perfusion and reperfusion of splanchnic organs and tumor tissue. *Lasers Surg. Med.* 20: 473–479.
- MacKintosh, F. C. and John, S. 1989. Diffusing-wave spectroscopy and multiple scattering of light in correlated random media. *Phys. Rev. B* 40: 2382–2406.
- Mahagne, M. H., David, O., Darcourt, J. et al. 2004. Voxel-based mapping of cortical ischemic damage using Tc 99m L,L-ethyl cysteinyl dimer SPECT in acute stroke. *J Neuroimaging* 14: 23–32.
- Maret, G. 1997. Diffusing-wave spectroscopy. *Curr. Opin. Colloid Interface Sci.* 2: 251–257.
- Maret, G. and Wolf, P. E. 1987. Multiple light scattering from disordered media. The effect of brownian motion of scatterers. *Z. Phys. B* 65: 409–413.
- Mehagnoul-Schipper, D. J., Van Der Kallen, B. F. W., Colier, W. et al. 2002. Simultaneous measurements of cerebral oxygenation changes during brain activation by near-infrared spectroscopy and functional magnetic resonance imaging in healthy young and elderly subjects. *Hum. Brain Mapp.* 16: 14–23.
- Menon, C., Polin, G. M., Prabakaran, I. et al. 2003. An integrated approach to measuring tumor oxygen status using human melanoma xenografts as a model. *Cancer Res.* 63: 7232–7240.
- Mesquita, R. C., Skuli, N., Kim, M. N. et al. 2010. Hemodynamic and metabolic diffuse optical monitoring in a mouse model of hindlimb ischemia. *Biomed. Opt. Express* 1(4): 1173–1187.
- Middleton, A. A. and Fisher, D. S. 1991. Discrete scatterers and autocorrelations of multiply scattered light. *Phys. Rev. B* 43: 5934–5938.
- Nielsen, A. N., Fabricius, M., and Lauritzen, M. 2000. Scanning laser-doppler flowmetry of rat cerebral circulation during cortical spreading depression. *J. Vasc. Res.* 37(6): 513–522.
- Patterson, M. S., Chance, B., and Wilson, B. C. 1989. Time resolved reflectance and transmittance for the non-invasive measurement of tissue optical properties. *Appl. Opt.* 28: 2331–2336.
- Petersen, E. T., Zimine, I., Ho, Y.C.L. & Golay, X. 2006. Non-invasive measurement of perfusion: A critical review of arterial spin labelling techniques. *Br. J. Radiol.* 79: 688–701.
- Pine, D. J., Weitz, D. A., Chaikin, P. M., and Herbolzheimer, E. 1988. Diffusing-wave spectroscopy. *Phys. Rev. Lett.* 60: 1134–1137.
- Rice, S. O. 1954. Mathematical analysis of random noise. In: *Noise and Stochastic Processes*, ed. N. Wax. New York: Dover, p. 133.
- Roche-Labarbe, N., Carp, S. A., Surova, A. et al. 2010. Noninvasive optical measures of CBV, StO₂, CBF Index, and rCMRO₂ in human premature neonates' brains in the first six weeks of life. *Hum. Brain Mapp.* 31(3): 341–352.
- Roland, P. E., Larsen, B., Lassen, N. A., and Skinhoj, E. 1980. Supplementary motor area and other cortical areas in organization of voluntary movements in man. *J. Neurophysiol.* 43: 118–136.
- Sehgal, C. M., Arger, P. H., Rowling, S. E. et al. 2000. Quantitative vascularity of breast masses by Doppler imaging: Regional variations and diagnostic implications. *J. Ultrasound Med.* 19: 427–40; quiz 441–442.
- Seitz, R. J. and Roland, P. E. 1992. Learning of sequential finger movements in man—a combined kinematic and positron emission tomography (PET) study. *Eur. J. Neurosci.* 4: 154–165.
- Shang, Y., Symons, T. B., Durduran, T. et al. 2010. Effects of muscle fiber motion on diffuse correlation spectroscopy blood flow measurements during exercise. *Biomed. Opt. Express* 1(2): 500–511.
- Shang, Y., Zhao, Y., Cheng, R. et al. 2009. Portable optical tissue flow oximeter based on diffuse correlation spectroscopy. *Opt. Lett.* 34: 3556–3558.
- Song, L., Li, H., Sunar, U. et al. 2007. Naphthalocyanine-reconstituted LDL nanoparticles for in vivo cancer imaging and treatment. *Int. J. Nanomed.* 2: 767–774.
- Stephen, M. J. 1988. Temporal fluctuations in wave propagation in random media. *Phys. Rev. B* 37: 1–5.
- Stern, M. D. 1975. In vivo evaluation of microcirculation by coherent light scattering. *Nature* 254: 56–58.
- Sunar, U., Makonnen, S., Zhou, C. et al. 2007. Hemodynamic responses to antivasular therapy and ionizing radiation assessed by diffuse optical spectroscopies. *Opt. Express* 15: 15507–15516.
- Sunar, U., Quon, H., Durduran, T. et al. 2006. Noninvasive diffuse optical measurement of blood flow and blood oxygenation for monitoring radiation therapy in patients with head and neck tumors: A pilot study. *J. Biomed. Opt.* 11(6): 064021–064021.
- Tanaka, T., Riva, C., and Ben-Sira, I. 1974. Blood velocity measurements in human retinal vessels. *Science* 186: 830–831.
- Tong, P., Goldberg, W. I., Chan, C. K., and Sirivat, A. 1988. Turbulent transition by photon-correlation spectroscopy. *Phys. Rev. A* 37: 2125–2133.

- Valkov, A. Y. and Romanov, V. P. 1986. Characteristics of propagation and scattering of light in nematic liquid crystals. *Sov. Phys. JETP* 63: 737–743.
- Varma, H. M., Nandakumaran, A. K., and Vasu, R. M. 2009. Study of turbid media with light: Recovery of mechanical and optical properties from boundary measurement of intensity autocorrelation of light. *J. Opt. Soc. Am. A Opt. Image Sci. Vis.* 26: 1472–1483.
- Wallace, D. J., Michener, B., Choudhury, D. et al. 1999. Summary of the results of a 95 subject human clinical trial for the diagnosis of peripheral vascular disease using a near infrared frequency domain hemoglobin spectrometer. *Proc. SPIE*: 300–316.
- Wang, H. W., Putt, M. E., Emanuele, M. J. et al. 2004. Treatment-induced changes in tumor oxygenation predict photodynamic therapy outcome. *Cancer Res.* 64: 7553–7561.
- Williams, D. S., Detre, J. A., Leigh, J. S., and Koretsky, A. P. 1992. Magnetic resonance imaging of perfusion using spin inversion of arterial water. *PNAS* 89: 212–216.
- Wintermark, M., Maeder, P., Verdun, F. R. et al. 2000. Using 80 kVp versus 120 kVp in perfusion CT measurement of regional cerebral blood flow. *Am. J. Neuroradiol.* 21: 1881–1884.
- Wintermark, M., Sesay, M., Barbier, E. et al. 2005. Comparative overview of brain perfusion imaging techniques. *Stroke* 36: 83–99.
- Wolf, M., Franceschini, M. A., Paunescu, L. A. et al. 2003. Absolute frequency-domain pulse oximetry of the brain: Methodology and measurements. *Adv. Exp. Med. Biol.* 530: 61–73.
- Wolf, R. L., Maret, G., Akkermans, E., and Maynard, R. 1988. Optical coherent backscattering by random media: An experimental study. *J. Phys. France* 49: 60–75.
- Xing, X., Mohler, E. R., Zhou, C. et al. 2007. Hemodynamic changes in diabetic pig muscle. *SVMB 18th Annual Meeting*, Baltimore, MA, 2007.
- Ye, F. Q., Yang, Y. H., Duyn, J. et al. 1999. Quantitation of regional cerebral blood flow increases during motor activation: A multislice, steady-state, arterial spin tagging study. *Magn. Reson. Med.* 42: 404–407.
- Yodh, A. G., Kaplan, P. D., and Pine, D. J. 1990. Pulsed diffusing-wave spectroscopy: High resolution through nonlinear optical gating. *Phys. Rev. B* 42: 4744–4747.
- Yu, G., Durduran, T., Furuya, D., Greenberg, J. H., and Yodh, A. G. 2003. Frequency-domain multiplexing system for in vivo diffuse light measurements of rapid cerebral hemodynamics. *Appl. Opt.* 42: 2931–2939.
- Yu, G., Durduran, T., Lech, G. et al. 2005a. Time-dependent blood flow and oxygenation in human skeletal muscles measured with noninvasive near-infrared diffuse optical spectroscopies. *J. Biomed. Opt.* 10: 024027.
- Yu, G., Durduran, T., Zhou, C. et al. 2005b. Noninvasive monitoring of murine tumor blood flow during and after photodynamic therapy provides early assessment of therapeutic efficacy. *Clin. Cancer Res.* 11: 3543–3552.
- Yu, G., Durduran, T., Zhou, C. et al. 2006. Real-time in situ monitoring of human prostate photodynamic therapy with diffuse light. *Photochem. Photobiol.* 82: 1279–1284.
- Yu, G., Floyd, T., Durduran, T. et al. 2007. Validation of diffuse correlation spectroscopy for muscle blood flow with concurrent arterial spin labeled perfusion MRI. *Opt. Express* 15: 1064–1075.
- Zhou, C. 2007. In-vivo optical imaging and spectroscopy of cerebral hemodynamics. PhD dissertation, University of Pennsylvania, Philadelphia, PA.
- Zhou, C., Choe, R., Shah, N. et al. 2007. Diffuse optical monitoring of blood flow and oxygenation in human breast cancer during early stages of neoadjuvant chemotherapy. *J. Biomed. Opt.* 12: 051903.
- Zhou, C., Eucker, S., Durduran, T. et al. 2009. Diffuse optical monitoring of hemodynamic changes in Piglet brain with closed head injury. *J. Biomed. Opt.* 14: 034015.
- Zhou, C., Yu, G., Furuya, D. et al. 2006. Diffuse optical correlation tomography of cerebral blood flow during cortical spreading depression in rat brain. *Opt. Express* 14: 1125–1144.
- Zirak, P., Delgado-Mederos, R., Martí-Fàbregas, J. et al. 2010. Effects of acetazolamide on the micro- and macro-vascular cerebral hemodynamics: A diffuse optical and transcranial doppler ultrasound study. *Biomed. Opt. Express* 1(5): 1443–1459.